Two-dimensional periodic structures modeling based on second strain gradient elasticity for a beam grid

Bo Yang, Abdelmalek Zine, Christophe Droz, Mohamed Ichchou

To cite this version:

Bo Yang, Abdelmalek Zine, Christophe Droz, Mohamed Ichchou. Two-dimensional periodic structures modeling based on second strain gradient elasticity for a beam grid. International Journal of Mechanical Sciences, 2022, 222, pp.1-13. 10.1016/j.ijmecsci.2022.107199 . hal-03622173

HAL Id: hal-03622173
https://hal.science/hal-03622173v1

Submitted on 28 Mar 2022

Two-dimensional periodic structures modeling based on second strain gradient elasticity for a beam grid

Bo Yang[a], Abdelmalek Zine[b], Christophe Droz[c,d], Mohamed Ichchou[a]

[a] *LTDS - CNRS UMR 5513, Vibroacoustics & Complex Media Research Group, École Centrale de Lyon, France*
[b] *Institute Camille Jordan – CNRS UMR 5208, École Centrale de Lyon, France*
[c] *KU Leuven, Department of Mechanical Engineering, DMMS-M Lab, Flanders Make, Belgium*
[d] *Univ. Gustave Eiffel, Inria, COSYS/SII, I4S Team, France*

Abstract

Higher order gradient elasticity theories are widely applied to determine the wave propagation characteristics of micro-sized structures. The novelty of this paper, firstly, is using the Second Strain Gradient (SSG) theory to explore the mechanism of a micro-sized 2D beam grid. The strong formulas of continuum model including governing equations and boundary conditions are derived by using the Hamilton principle. Then, a valuable long-range Lattice Spring Model (LSM) is elaborated, providing a reasonable explanation for the model based on SSG theory. The dynamic continuum equations from LSM are calculated through the Fourier series transform approach. Finally, the dynamic properties of 2D beam grid are analyzed within the Wave Finite Element Method (WFEM) framework. The band structure and slowness surfaces, confined to the irreducible first Brillouin zone, are studied in frequency spectrum. The energy flow vector fields and wave beaming effects are discussed through SSG theory and Classical Theory (CT) of elasticity. The results show that the proposed approach is of significant potential for investigating the 2D wave propagation characteristics of complex micro-sized periodic structures.

Key words: Wave finite element method, second strain gradient theory, band structure, energy flow vector fields, wave beaming effects

1. Introduction

Periodic structures which are constructed by repeating a basic unit cell to form regular patterns are widely used in engineering fields. Initially, studies focused on the field of solid-state physics at macro-sized level based on Classical Theory (CT) of elasticity [1, 2]. For instance, the characteristics of fatigue issues and acoustic radiation for periodic systems need to be known in engineering applications [3]. The analysis of wave propagation is of great significance in engineering application [4, 5]. The study of maximizing and localizing band gaps or stop bands in some specific frequency ranges has also attracted many researchers [6, 7].

Recently, the exploration for micro-sized structures, such as periodically positioned nano-sized Silicon resonator [8], nanobio-sensors [9] and nano-beams [10, 11, 12] has become a hot spot. Ebrahimi [13] studied wave propagation characteristics in heterogeneous nano-beams by employing a new two-step porosity-dependent homogenization scheme. Then, he explored the effects of magnetic field on thermally affected propagation of acoustical waves in rotary double-nanobeam systems [14]. Dabbagh [15] analyzed the post-buckling behaviors of multi-scale hybrid nano-composite beam-type structures. The micro-sized structure has the property of size effects which is different from macro-sized structure. Generally, there exist three major aspects of sized effects. The first is large surface-volume ratio. The micro-particles such as atoms with associated energy on the surface of the structure produce surface tension which can not be ignored in micro-structures [16, 17]. The second is micro-material in the structure. In addition to the macro-deformations caused by macro-material in the structure, the micro-deformations such as micro-rotation, micro-stretch caused by micro-material in the structure have important influences on the mechanical behavior of the structure [16]. Last, besides the local interaction property, there exist non-local interaction property in the micro-sized structure [18, 19].

Because of the existence of size effects, the mechanical behaviors of micro-structure are significantly different from the macro-structure. In order to solve the problems mentioned above, the non-classical continuum theories of elasticity have been proposed. In general, these theories can be categorized into four different classes namely the strain gradient family, micro-continuum theory, non-local elasticity theory and surface elasticity theory. The strain gradient family is composed of couple stress theory, modified couple stress theory, first and second strain gradient theories. In couple stress theory proposed by Toupin [20], Mindlin, Tiersten [21] and Koiter [22], in addition to the conventional deformations, the gradient of rotation vector is considered in the strain energy as well. In modified couple stress theory put forward by Yang [23], the couple stress tensor is assumed to be symmetric by introducing an equilibrium condition of moments of couples. Mindlin established First Strain Gradient (SG) theory [24] in which the potential energy density composed of strain and first gradient of strain is considered; but only for micro-sized noncentro-symmetric materials [25]. In order to explore the properties of centro-symmetric materials, the Second Strain Gradient (SSG) theory [26] was put forward, which offers a reasonable explanation for the transforming of strain or tension on a solid plane surface. The potential energy density in SSG theory is a function of strain, first gradient of strain and second gradient of strain. The equilibrium equation is a high order partial differential equation with classical and non-classical boundary conditions.

Furthermore, the micro-continuum theory was established by Eringen [27] consisting of micro-polar theory, micro-stretch theory and micro-morphic theory. In micro-polar theory, the independent rotation scalar of micro-material is considered. In micro-stretch theory, the independent stretch scalar of micro-material is considered. Micro-morphic theory is the most general one in which the micro-material in the structure can rotate and deform independently. In non-local elasticity theory initiated by Kroner [28], the stress at a point in a continuum depends on the strains at all points of the body. Gurtin [29] proposed the mostly used model of the surface elasticity, in which a scalar coefficient interpreted as a residual surface tension is considered.

In order to derive the mathematical and mechanical models including governing equations and boundary conditions for micro-sized systems, SSG theory is widely applied and some important results are elaborated. For example, Delfani [30] employed Mindlin's SSG elasticity to extract an estimate of the effective shear modulus of an anti-plane mode. It shows that, at a constant volume fraction, the shear modulus of the composite takes a higher value when the diameter of the fibers decreases. Khakalo [31] derived the fundamental equations for Form II of Mindlin's SSG elasticity theory for isotropic materials. It is remarkable that the calibrated higher-order parameters keep the strain energy density positive definite. What is more, Esen [32] applied the nonlocal strain gradient theory with the weak form finite element method, and presented the moving mass problem in the literature for micro-capillary Timoshenko beams. A nonlocal strain gradient modeling for symmetric and also antisymmetric sandwich plates are presented by Sadegh [33].

On the other hand, Lattice Spring Model (LSM) theory [34] is also a valuable approach to interpret the dynamic characteristics for micro-sized medias. One of its applications is the investigation of wave propagation within linear strain-gradient elasticity for a 2D lattice structure [35]. The continuum equation of motion with derivatives can be determined by long-range interactions in LSM. For example, Polyzos [36] calculated the continuum equation of a mass-spring lattice longitudinal model formed by nearest, next-nearest interactions between different mass nodes. This LSM can only be used to describe the SG theory whose continuum equation of motion contains one higher order term. Different from SG theory, the continuum equation of motion for SSG theory contains two higher order terms, the LSM of nearest, next-nearest interactions is insufficient to derive this two higher order terms. So the establishment of LSM with nearest, next-nearest and next-next-nearest interactions is necessary to determine the continuum equation under SSG theory. The LSM for SSG theory is a new research topic, especially for bending and torsion vibration. If only the nearest interaction is considered, the LSM will reverse to the one by CT. LSM is widely used in wave propagation analysis, For example, Russillo [37] modelled the small-size 2D beam lattice by stress-driven nonlocal Rayleigh beam theory. Hu [38] studies the propagation and attenuation of blasting wave induced by explosion in underground rock cavern by employing the newly developed four-dimensional lattice spring model. In addition, a comparison is made between two-dimensional elastic discrete lattices and a corresponding Cosserat continuum to study wave propagation characteristics by Suiker [39]. Zhu [40] performed a validation study of the distinct lattice spring model (DLSM) for wave propagation problems.

However, there exist difficulties to interpret the dynamical properties of complex periodic structures through the analytical methods, especially for the micro-sized medias. In the last decade, numerical methods that can explore complex structures received a lot of attention [41, 42, 43]. Among them, the Wave Finite Element Method (WFEM) [44, 45] is an effective tool that combines periodic structure theory [46] with commercial FE packages to analyze the wave propagation characteristics of complex structures. WFEM is based on the spectral study of a single unit cell to reflect the dynamic characteristics of the entire periodic structure [47]. The resulting mass and stiffness matrices are post-processed to establish the dynamic stiffness matrix of the unit cell.

WFEM has been widely used to explore and elaborate the dynamic problems in engineering applications. The author utilized SSG theory within WFEM framework to study 1D wave propagation characteristic of Euler-Bernoulli bending beam and torsional beam for the first time [34]. However, as we all know, the propagation characteristics of waves in realistic periodic structures is very complicated. The potential dynamic properties of complex structures cannot be obtained by studying 1D waves only. So, the exploration of 2D waves in complex structures is of great significance. For instance, the slowness surfaces and wave beaming effects that can reflect the characteristics of 2D waves play an important role in the design and optimization of complex acoustic materials. Some studies focus on the dispersion computation of 2D periodic systems [48] and analysis of curved structures [49]. In addition, Errico [50] built the flow-induced vibrations of periodic flat and axial-symmetric structures with a wave-based method. A wave-based optimization framework for 1D and 2D periodic structures are introduced by Boukadia [51]. Singh presented a stochastic quadratic eigenvalue formulation for the 1D and 2D periodic medias. The result shows that the obtained computational cost savings can be a remarkable achievement for the optimization study of complex structures.

The main objective of this work is, firstly, to illustrate the strong and weak forms of a 2D micro-sized beam grid based on SSG theory, and, secondly, to study the 2D waves properties of this beam grid within the WFEM framework. The reason for combining WFEM with SSG theory is that the characteristics of micro-sized medias can be interpreted by SSG theory and the dynamical properties of complex periodic structures can be investigated through WFEM.

So as to study the dynamic characteristics of micro-sized periodic structures, this article begins with the derivation of strain potential energy, kinetic energy and work done by external forces based on SSG theory. Then, strong formulas considering higher-order parameters are calculated through the Hamilton principle. The Lagrange equation is used to determine the displacement component expression in LSM formed by interactions of nearest, next-nearest and next-next-nearest neighbors. According to the Fourier series transform approach, LSM is transformed into continuum model under the condition that the number of mass nodes in LSM is large enough. Weak formulas including element stiffness and mass matrices are deduced by using the higher order Hermite interpolation functions.

This paper is organized as follow: in section 2, a beam grid is presented as 2D periodic structures. The analysis is restricted to out-of plane vibration including bending and torsion. A continuum model and long-range LSM are introduced. Strong formulas of the beam grid are established based on SSG theory. Afterwards, in section 3, the weak formulas of an element are illustrated and the global dynamic stiffness matrix of a unit cell is assembled. WFEM inverse form for 2D periodic systems is introduced. Dynamic behaviors of the beam grid such as band structure, slowness surfaces, energy flow vector fields and wave beaming effects are discussed in section 4. Ultimately, some useful conclusions are shown in section 5.

2. Strong formulas for out-of plane vibration

In order to analyze the dynamical problems of a 2D beam grid, the strong formulas of the beam grid should be confirmed firstly. In this part, starting with the introduction of SSG theory. Then, a continuum model which is restricted to out-of plane vibration is established. The governing equation is derived through the Hamilton's principle. Finally, a LSM of the beam grid is proposed, which offers a reasonable explanation for Mindlin's SSG theory, and the dynamic continuum equation is illustrated based on Fourier series transform.

2.1. A brief of Second Strain Gradient (SSG) theory

According to the SSG theory proposed by Mindlin [26], the strain energy density $\overline{\mathcal{U}}$ for isotropic linear elastic materials is a function of strain tensor $\boldsymbol{\varepsilon}$, first gradient of the strain tensor $\boldsymbol{\xi}=\nabla\boldsymbol{\varepsilon}$ and second gradient of the strain tensor $\boldsymbol{\zeta}=\nabla\nabla\boldsymbol{\varepsilon}$, as below:

$$\begin{aligned}\overline{\mathcal{U}} =&\frac{1}{2}\lambda(\mathrm{tr}\,\boldsymbol{\varepsilon})^2 + \mu\boldsymbol{\varepsilon} : \boldsymbol{\varepsilon} + a_1(\nabla\cdot\boldsymbol{\varepsilon})\cdot\nabla(\mathrm{tr}\,\boldsymbol{\varepsilon}) + a_2\nabla(\mathrm{tr}\,\boldsymbol{\varepsilon})\cdot\nabla(\mathrm{tr}\,\boldsymbol{\varepsilon}) + a_3(\nabla\cdot\boldsymbol{\varepsilon})\cdot(\nabla\cdot\boldsymbol{\varepsilon})\\ &+ a_4\nabla\boldsymbol{\varepsilon}\,\vdots\,\nabla\boldsymbol{\varepsilon} + a_5\nabla\boldsymbol{\varepsilon}\,\vdots\,\boldsymbol{\varepsilon}\nabla + b_1(\Delta\mathrm{tr}\,\boldsymbol{\varepsilon})^2 + b_2\nabla\nabla(\mathrm{tr}\,\boldsymbol{\varepsilon}) : \nabla\nabla(\mathrm{tr}\,\boldsymbol{\varepsilon}) + b_3\Delta\boldsymbol{\varepsilon} : \nabla\nabla(\mathrm{tr}\,\boldsymbol{\varepsilon})\\ &+ b_4\Delta\boldsymbol{\varepsilon} : \Delta\boldsymbol{\varepsilon} + b_5\nabla\cdot\boldsymbol{\varepsilon}\nabla : \nabla\boldsymbol{\varepsilon}\cdot\nabla + b_6\nabla\nabla\boldsymbol{\varepsilon} :: \nabla\nabla\boldsymbol{\varepsilon} + b_7\nabla\nabla\boldsymbol{\varepsilon} :: \nabla\boldsymbol{\varepsilon}\nabla + c_1(\mathrm{tr}\,\boldsymbol{\varepsilon})\Delta(\mathrm{tr}\,\boldsymbol{\varepsilon})\\ &+ c_2\boldsymbol{\varepsilon} : \nabla\nabla(\mathrm{tr}\boldsymbol{\varepsilon}) + c_3\boldsymbol{\varepsilon} : \Delta\boldsymbol{\varepsilon},\end{aligned} \tag{1}$$

where a_i, b_i and c_i represent the higher order parameters. Scalar products between vectors or tensors are defined as: $\boldsymbol{\varepsilon} : \boldsymbol{\varepsilon}=\varepsilon_{ij}\varepsilon_{ij}$, $\nabla\boldsymbol{\varepsilon}\,\vdots\,\nabla\boldsymbol{\varepsilon}=\varepsilon_{jk,i}\varepsilon_{jk,i}$, $\nabla\nabla\boldsymbol{\varepsilon} :: \nabla\nabla\boldsymbol{\varepsilon}=\varepsilon_{kl,ij}\varepsilon_{kl,ij}$. $\boldsymbol{\varepsilon}=sym(\nabla\mathbf{U})$ where $\mathbf{U}$ denotes displacement fields vector. *Lamé* parameters λ and μ have relations with Young's modulus E, shear modulus G and Poisson's ratio ν, as $G = \mu = E/2(1+\nu), \lambda = E\nu/(1+\nu)(1-2\nu)$. The higher order parameters mentioned above for material Aluminum (Al) [25] are shown in Tab. 1.

Table 1: Parameters a_i ($eV/\text{Å}$), b_i ($eV{\cdot}\text{Å}$) and c_i ($eV/\text{Å}$) for Aluminum.

a_1	a_2	a_3	a_4	a_5	b_1	b_2	b_3	b_4	b_5
0.1407	0.0027	-0.0083	0.0966	0.2584	0.7927	0.0644	-0.1943	-0.0009	0.0009
b_6	b_7	c_1	c_2	c_3					
16.1566	48.5291	0.5041	0.3569	0.1782					

2.2. *Continuum model*

As shown in Fig. 1(a), a beam grid is presented as a 2D periodic structure. The dynamical properties of whole beam grid can be reflected through the spectral analysis of a unit cell in framework of WFEM [44]. Starting with the dynamical analysis of the beam along x direction in the unit cell as shown in Fig. 1(b). According to the out-of plane vibration analysis [52], the vibration of beam is restricted to bending and torsion. The calculating process of strong formulas for continuum model is shown in Fig. 2. All the details for illustrating the governing equations and boundary conditions of bending and torsion cases can be found in the author's paper [34] and main derivation results are cited in this work. Here should be noted that, the effects of shear deformation are ignored, so the model in this work cannot be employed for thick structures whose properties are influenced by shear deformation.

Firstly, the beam along x direction in the unit cell is regarded as a Euler-Bernoulli micro-sized bending beam with displacements w along z direction and angle θ in $x0z$ plane. The variational principle is applied to derive the governing equation. Consider a lateral distributed force $\overline{f}(x,t)$ along z direction acting on the beam. Here should be pointed that there are two main reasons for not considering micro-inertia. First, as introduced by Mindlin [24], the mass consists of two parts in micro-structure. First part comes from macro-material per unit volume which is the majority part. Second part called non-classical part comes from micro-material per unit volume whose proportion is very small. In second strain gradient theory, the main influence on the mechanical properties of the micro-structure comes from the higher-order strain terms in the strain energy density and macro-inertia per unit volume. The influence of micro-inertia appears especially at high frequency [53], whose proportion, however, is secondary compared to macro-inertia and are often omitted [54]. Second, the material used in this work is pure Aluminum with the large identical crystal grains. Other micro-materials in the crystal can be considered absent. So for this reason, the micro-inertia from micro-material was ignored in this work. Some applications can be found in [55, 56, 57]. According to the calculating process in Fig. 2, the displacements u_1, u_2 and u_3 along x, y and z directions respectively can be confirmed based on Euler beam theory [34]. Then, nonzero components of first, second and third gradient of displacement can be derived through SSG theory. Finally, the governing equation for bending can be deduced by Hamilton formula and the details for confirming ε, ξ and ζ are presented in A, one obtains:

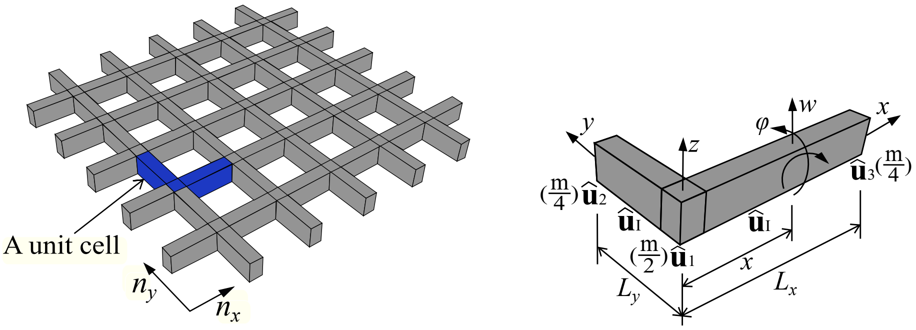

(a) A beam grid.

(b) A unit cell of the beam grid.

Figure 1: Sketch of 2D beam grid and unit cells. Three displacements at position x on a branch of the unit cell: displacement w along z direction, angle θ in $x0z$ plane and angle φ in $y0z$ plane, $\hat{\mathbf{u}}_{1,2,3}$ is corner DOFs, $\hat{\mathbf{u}}_\text{I}$ is internal DOFs.

$$C_1^b \frac{\partial^4 w(x,t)}{\partial x^4} + (C_4^b - C_2^b)\frac{\partial^6 w(x,t)}{\partial x^6} + C_3^b \frac{\partial^8 w(x,t)}{\partial x^8} - \overline{f}(x,t) = \rho A \frac{\partial^2 w(x,t)}{\partial t^2}. \tag{2}$$

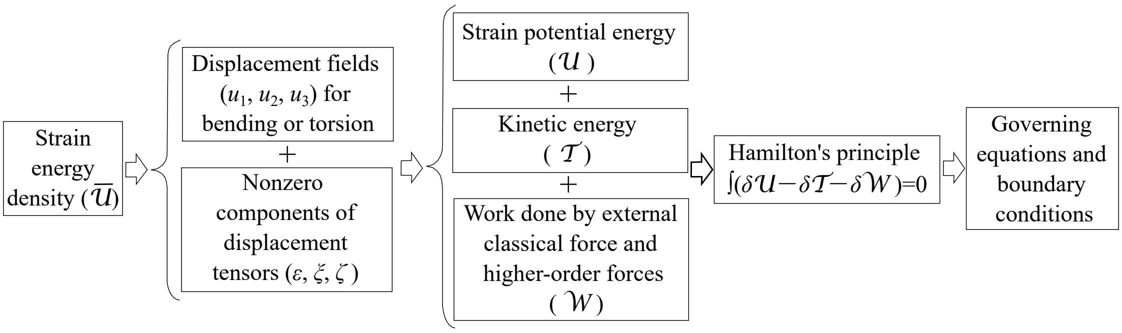

Figure 2: Graphical representation for analyzing continuum model vibration. u_1, u_2 and u_3 are the displacements along x, y and z direction respectively. ε, ξ and ζ are nonzero components of first, second and third gradient of displacement tensors respectively. Utilizing the Hamilton formula composed of strain potential energy, kinetic energy and work done by forces, the governing equations and boundary conditions can be calculated.

where $C_1^b = 2(a_1 - a_2 + a_3 + 3a_4 - a_5)A + EI$, $C_2^b = 2(a_1 + a_2 + a_3 + a_4 + a_5)I + 4(b_2 - b_4 + b_5 + 2b_6)A$, $C_3^b = 2(b_1 + b_2 + b_3 + b_4 + b_5 + b_6 + b_7)I$, $C_4^b = 3(c_1 + c_2 + c_3)I$, A is the cross section area of the beam, I is the bending moment of inertia. Simultaneously, the boundary conditions for micro-sized Euler-Bernoulli beam on the end-section (i.e. $x = 0, L_x$) are extracted by SSG theory:

$$\begin{aligned}
&-C_1^b\frac{\partial^3 w(x,t)}{\partial x^3} - (C_4^b - C_2^b)\frac{\partial^5 w(x,t)}{\partial x^5} - C_3^b\frac{\partial^7 w(x,t)}{\partial x^7} = f_0 \text{ or } \delta w(x,t) = 0;\\
&-C_1^b\frac{\partial^2 w(x,t)}{\partial x^2} - (C_4^b - C_2^b)\frac{\partial^4 w(x,t)}{\partial x^4} + C_3^b\frac{\partial^6 w(x,t)}{\partial x^6} = M_0 \text{ or } \delta\frac{\partial w(x,t)}{\partial x} = 0;\\
&-(\frac{1}{2}C_4^b - C_2^b)\frac{\partial^3 w(x,t)}{\partial x^3} + C_3^b\frac{\partial^5 w(x,t)}{\partial x^5} = M_1 \text{ or } \delta\frac{\partial^2 w(x,t)}{\partial x^2} = 0;\\
&\frac{1}{2}C_4^b\frac{\partial^2 w(x,t)}{\partial x^2} + C_3^b\frac{\partial^4 w(x,t)}{\partial x^4} = M_2 \text{ or } \delta\frac{\partial^3 w(x,t)}{\partial x^3} = 0,
\end{aligned} \tag{3}$$

where f_0 and M_0 are classical loads, $M_{1,2}$ denotes higher order load on the end-section of the beam.

Next, the beam is regarded as a torsional beam with angle φ in $y0z$ plane. A distributed torque $\overline{T}(x,t)$ around x axis is considered. In order to derive the strong formulas of torsional vibration, the variational principle is used and the calculating process is shown in B. Here, the non-classical part of kinetic energy is ignored in the calculation of governing equation [54] as well, one arrives:

$$C_1^t\frac{\partial^2\varphi(x,t)}{\partial x^2} + (C_4^t - C_2^t)\frac{\partial^4\varphi(x,t)}{\partial x^4} + C_3^t\frac{\partial^6\varphi(x,t)}{\partial x^6} - \overline{T}(x,t) = \rho J\frac{\partial^2\varphi(x,t)}{\partial t^2}. \tag{4}$$

where $C_1^t = GJ + 2A(4a_4 - a_5)$, $C_2^t = J(a_3 + a_4)/2 - 2A(b_4 + 2b_5 - 6b_6 + 2b_7)$, $C_3^t = 2J(b_5 + b_6)$, $C_4^t = Jc_3$, J is the torsional moment of inertia in plane $y0z$. The boundary conditions for micro-sized torsional beam on the end-section (i.e. $x = 0, L_x$) are extracted :

$$\begin{aligned}
&C_1^t\frac{\partial\varphi(x,t)}{\partial x} + (C_4^t - C_2^t)\frac{\partial^3\varphi(x,t)}{\partial x^3} + C_3^t\frac{\partial^5\varphi(x,t)}{\partial x^5} = T_0 \text{ or } \delta\varphi(x,t) = 0;\\
&(C_2^t - \frac{1}{2}C_4^t)\frac{\partial^2\varphi(x,t)}{\partial x^2} + C_3^t\frac{\partial^4\varphi(x,t)}{\partial x^4} = T_1 \text{ or } \delta\frac{\partial\varphi(x,t)}{\partial x} = 0;\\
&\frac{1}{2}C_4^t\frac{\partial\varphi(x,t)}{\partial x} + C_3^t\frac{\partial^3\varphi(x,t)}{\partial x^3} = T_2 \text{ or } \delta\frac{\partial^2\varphi(x,t)}{\partial x^2} = 0,
\end{aligned} \tag{5}$$

where the classical and higher-order loads on the end-section of the torsional micro-beam can be represented by T_0 and $T_{1,2}$ respectively.

2.3. Lattice Spring Model (LSM)

As shown in Fig. 3, the discrete structure, formed by interactions of nearest, next-nearest and next-next-nearest neighbors, is a valuable presentation for SSG model. The distance d is a numerical parameter which is used for the convergence study [55]. The process of dynamic analysis for bending and torsion is presented in Fig. 4. The lattice equation of motion for displacement field on node n is illustrated from the LSM method. After Fourier series transform [58], the dynamic continuum equations for bending and torsion will be derived separately.

Starting with the bending analysis within the LSM framework, the branch of the unit cell along x direction, as shown in Fig. 3, is regarded as a discrete form of Euler–Bernoulli beam based on SSG theory. The coupling constants from nearest (red line), next-nearest (blue line) and next-next-nearest (green line) neighbors interactions can be expressed by k_1^b, k_2^b and k_3^b which are called bending stiffness. The degree of freedoms (DOFs) on node n are displacement w along z direction and angle of rotation θ in $x0z$ plane. The length d is extremely short and nodes number P should be large enough. The lattice function of motion on node n can be calculated according to displacement component (θ, w) expression and Lagrange equation, with detail in C, one arrives:

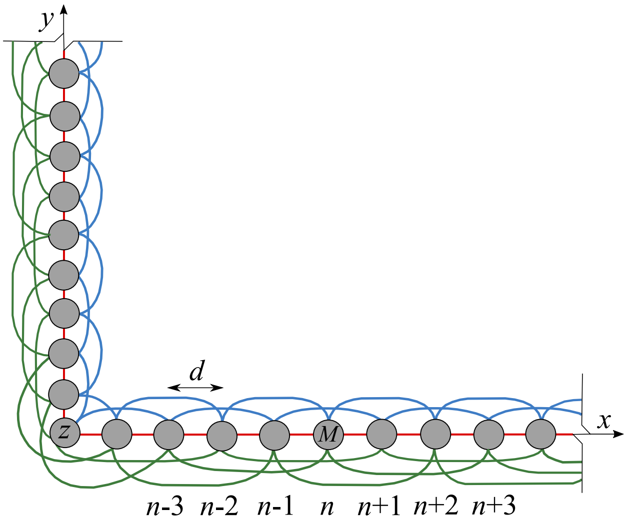

Figure 3: A unit cell by LSM with three coupling relations. Red line denotes the nearest neighbor interaction, blue line means the next-nearest neighbor interaction and green line represents the next-next-nearest neighbor interaction. d is the distance between two nodes and the mass $M = \rho A d$. z axis is perpendicular to $x0y$ plane.

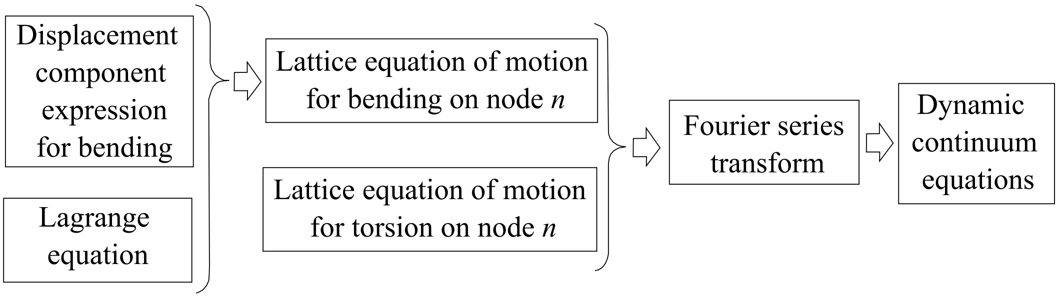

Figure 4: Graphical representation for analyzing LSM vibration. Lattice equation of motion on node n is confirmed according to displacement component and dynamic continuum equation is derived through Fourier series transform approach.

$$\begin{aligned}&\frac{k_1^b}{d^3}\left(w_{n-2}-4w_{n-1}+6w_n-4w_{n+1}+w_{n+2}\right)+\frac{k_2^b}{(2d)^3}\left(w_{n-4}-4w_{n-2}+6w_n-4w_{n+2}+w_{n+4}\right)\\&+\frac{k_3^b}{(3d)^3}\left(w_{n-6}-4w_{n-3}+6w_n-4w_{n+3}+w_{n+6}\right)-f_n=M\frac{\mathrm{d}^2w_n(t)}{\mathrm{d}t^2},\end{aligned}\tag{6}$$

where w_i is the displacement along z direction on node i ($n-6, n-4, n-3, n-2, n-1, n, n+1, n+2, n+3, n+4, n+6$), f_n is an external force loaded on node n along z direction. The expression of $w(x,t)$ can be illustrated based on Fourier series transform approach (C), as expressed:

$$\begin{aligned}&L_4^b\frac{\partial^4 w(x,t)}{\partial x^4}+L_6^b\frac{\partial^6 w(x,t)}{\partial x^6}+L_8^b\frac{\partial^8 w(x,t)}{\partial x^8}+o\left(L_j^b\frac{\partial^j w(x,t)}{\partial x^j}\right)-\overline{f}(x,t)\\&=\rho A\frac{\partial^2 w(x,t)}{\partial t^2},(j=10,12,...),\end{aligned}\tag{7}$$

with $L_4^b=k_1^b+2k_2^b+3k_3^b$, $L_6^b=-\left(\frac{k_1^b}{6}+\frac{4k_2^b}{3}+\frac{9k_3^b}{2}\right)d^2$, $L_8^b=\left(\frac{k_1^b}{80}+\frac{2k_2^b}{5}+\frac{243k_3^b}{80}\right)d^4$, $L_{10}^b=-\left(\frac{17k_1^b}{30240}+\frac{68k_2^b}{945}+\frac{1377k_3^b}{1120}\right)d^6$,...

Ignore the higher order infinitesimal part o in Eq. 7 and assume that the first three parts in the left side of the equation above are equal to the corresponding parts in Eq. 2 which is derived from Mindlin's theory. The continuum equation for micro-sized Euler–Bernoulli lattice bending beam can be confirmed and the relations between bending stiffness and higher order parameters can be calculated.

Next, the branch of the unit cell along x direction is regarded as a lattice torsional beam, as shown in Fig. 3, the three coupling parameters from the interactions of nearest, next-nearest and next-next-nearest neighbors are represented by torsional stiffness k_1^t, k_2^t and k_3^t. The lattice function of motion on node n is expressed as:

$$k_1^t(\varphi_{n-1}-2\varphi_n+\varphi_{n+1})+k_2^t(\varphi_{n-2}-2\varphi_n+\varphi_{n+2})+k_3^t(\varphi_{n-3}-2\varphi_n-\varphi_{n+3})-T_n=\frac{MJ}{A}\frac{\mathrm{d}^2\varphi_n(t)}{\mathrm{d}t^2},\tag{8}$$

where φ_i is the angle around x axis on node i ($n-3, n-2, n-1, n, n+1, n+2, n+3$), T_n is an external torsional force loaded on node n around x axis. The expression of $\varphi(x,t)$ from the torsional LSM can be obtained, with the derivation process addressed in D, one arrives:

$$\begin{aligned}&L_2^t\frac{\partial^2 \varphi(x,t)}{\partial x^2}+L_4^t\frac{\partial^4 \varphi(x,t)}{\partial x^4}+L_6^t\frac{\partial^6 \varphi(x,t)}{\partial x^6}+o\left(L_j^t\frac{\partial^j \varphi(x,t)}{\partial x^j}\right)-\bar{T}(x,t)\\&=\rho J\frac{\mathrm{d}^2 \varphi(x,t)}{\mathrm{d}t^2},(j=8,10,...),\end{aligned}\tag{9}$$

with $L_2^t=(k_1^t+4k_2^t+9k_3^t)d$, $L_4^t=\left(\frac{k_1^t}{12}+\frac{4k_2^t}{3}+\frac{27k_3^t}{4}\right)d^3$, $L_6^t=\left(\frac{k_1^t}{360}+\frac{8k_2^t}{54}+\frac{81k_3^t}{40}\right)d^5$, $L_8^t=\left(\frac{7k_1^t}{20160}+\frac{4k_2^t}{315}+\frac{729k_3^t}{2240}\right)d^7$,...

Remove the higher order infinitesimal part o and the first three partial differential term coefficients are equal to the corresponding parts in Eq. 4. The continuum equation of torsional beam by LSM can be confirmed and the relations between the torsional stiffness and higher order parameters can be derived.

3. Wave Finite Element Method (WFEM)

After obtaining the strong formulas of the beam grid, the weak formulas then need to be determined. In this section, firstly, the element mass matrix, stiffness matrix and force vector are illustrated by using Hermite interpolation functions. Subsequently, the dynamical equation of a unit cell is defined within WFEM framework, which provides a way to analyze the wave propagation in 2D periodic structures.

3.1. *Finite element procedure*

In this part, the weak formulas for out-of plane vibration are transformed from strong formulas. As shown in Fig. 5, nodal displacement field for an element is:

$$\mathbf{u}^{(e)}(t)=\left[w_1,\varphi_1,\theta_1,\frac{\partial\varphi_1}{\partial x},\frac{\partial^2 w_1}{\partial x^2},\frac{\partial^2\varphi_1}{\partial x^2},\frac{\partial^3 w_1}{\partial x^3},w_2,\varphi_2,\theta_2,\frac{\partial\varphi_2}{\partial x},\frac{\partial^2 w_2}{\partial x^2},\frac{\partial^2\varphi_2}{\partial x^2},\frac{\partial^3 w_2}{\partial x^3}\right]^T,\tag{10}$$

in which the four DOFs, w_i, θ_i, $\frac{\partial^2 w_i}{\partial x^2}$, $\frac{\partial^3 w_i}{\partial x^3}$, $i=1,2$, belong to bending on each node and the three DOFs, φ_i, $\frac{\partial\varphi_i}{\partial x}$, $\frac{\partial^2\varphi_i}{\partial x^2}$, $i=1,2$, belong to torsion on each node. Then, defining bending displacement $w(x,t)$ and torsion displacement $\varphi(x,t)$ on

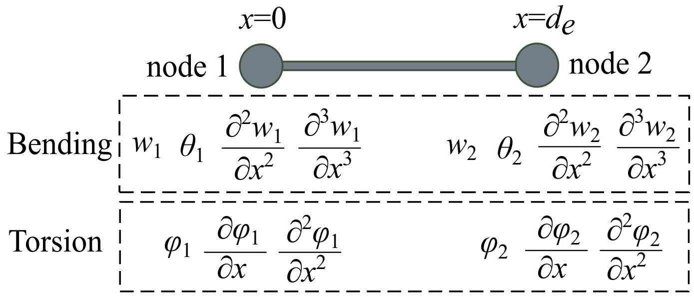

Figure 5: Two nodes fourteen DOFs in an element. For bending, there are four DOFs on each node including two conventional DOFs and two higher order DOFs. For torsion, there exist three DOFs on each node including one conventional DOFs and two higher order DOFs.

point $x \in \mathbb{R}^2$ inside an element:

$$\begin{aligned}
&\begin{pmatrix} w(x,t) \\ \varphi(x,t) \end{pmatrix} = \begin{pmatrix} \mathbf{N}^b(x) \\ \mathbf{N}^t(x) \end{pmatrix} \mathbf{u}^{(e)}(t) \\
&= \begin{bmatrix} \mathrm{N}_1^{b0}, & 0, & \mathrm{N}_1^{b1}, & 0, & \mathrm{N}_1^{b2}, & 0, & \mathrm{N}_1^{b3}, & \mathrm{N}_2^{b0}, & 0, & \mathrm{N}_2^{b1}, & 0, & \mathrm{N}_2^{b2}, & 0, & \mathrm{N}_2^{b3} \\ 0, & \mathrm{N}_1^{t0}, & 0, & \mathrm{N}_1^{t1}, & 0, & \mathrm{N}_1^{t2}, & 0, & 0, & \mathrm{N}_2^{t0}, & 0, & \mathrm{N}_2^{t1}, & 0, & \mathrm{N}_2^{t2}, & 0 \end{bmatrix} \mathbf{u}^{(e)}(t),
\end{aligned} \tag{11}$$

where the size of $\mathbf{N}^b$ is $1 \times p$ in which p is the number of DOFs for bending. $\mathbf{N}^t$ has the size of $1 \times r$ in which r is the number of DOFs for torsion.

In order to obtain the shape functions $\mathbf{N}^b$ for bending and $\mathbf{N}^t$ for torsion, the C^3 and C^2 continuum Hermite interpolation functions [34, 59, 60] guaranteeing the displacement and strain fields continuous and smooth at higher-order level are utilized in Eq. 11, as expressed:

$$\begin{aligned}
\mathrm{N}_1^{b0} &= 1 - 35\frac{x^4}{d_e^4} + 84\frac{x^5}{d_e^5} - 70\frac{x^6}{d_e^6} + 20\frac{x^7}{d_e^7}, \mathrm{N}_2^{b0} = 35\frac{x^4}{d_e^4} - 84\frac{x^5}{d_e^5} + 70\frac{x^6}{d_e^6} - 20\frac{x^7}{d_e^7}, \\
\mathrm{N}_1^{b1} &= x - 20\frac{x^4}{d_e^3} + 45\frac{x^5}{d_e^4} - 36\frac{x^6}{d_e^5} + 10\frac{x^7}{d_e^6}, \mathrm{N}_2^{b1} = -15\frac{x^4}{d_e^3} + 39\frac{x^5}{d_e^4} - 34\frac{x^6}{d_e^5} + 10\frac{x^7}{d_e^6}, \\
\mathrm{N}_1^{b2} &= \frac{x^2}{2} - 5\frac{x^4}{d_e^2} + 10\frac{x^5}{d_e^3} - 15\frac{x^6}{d_e^4} + 2\frac{x^7}{d_e^5}, \mathrm{N}_2^{b2} = 5\frac{x^4}{d_e^2} - 7\frac{x^5}{d_e^3} + 13\frac{x^6}{d_e^4} - 2\frac{x^7}{d_e^5}, \\
\mathrm{N}_1^{b3} &= \frac{x^3}{6} - 2\frac{x^4}{3d_e} + \frac{x^5}{d_e^2} - 2\frac{x^6}{3d_e^3} + \frac{x^7}{6d_e^4}, \quad \mathrm{N}_2^{b3} = -\frac{x^4}{6d_e} + \frac{x^5}{2d_e^2} - \frac{x^6}{2d_e^3} + \frac{x^7}{6d_e^4}, \\
\mathrm{N}_1^{t0} &= 1 - 10\frac{x^3}{d_e^3} + 15\frac{x^4}{d_e^4} - 6\frac{x^5}{d_e^5}, \qquad \mathrm{N}_2^{t0} = 10\frac{x^3}{d_e^3} - 15\frac{x^4}{d_e^4} + 6\frac{x^5}{d_e^5}, \\
\mathrm{N}_1^{t1} &= \frac{x}{d_e} - 6\frac{x^3}{d_e^3} + 8\frac{x^4}{d_e^4} - 3\frac{x^5}{d_e^5}, \qquad \mathrm{N}_2^{t1} = -4\frac{x^3}{d_e^3} + 7\frac{x^4}{d_e^4} - 3\frac{x^5}{d_e^5}, \\
\mathrm{N}_1^{t2} &= \frac{x^2}{2d_e^2} - 3\frac{x^3}{2d_e^3} + 3\frac{x^4}{2d_e^4} - \frac{x^5}{2d_e^5}, \qquad \mathrm{N}_2^{t2} = \frac{x^3}{2d_e^3} - \frac{x^4}{d_e^4} + \frac{x^5}{2d_e^5},
\end{aligned} \tag{12}$$

where the subscript number of $\mathbf{N}$ denotes the node number, superscript number means the derivative order with respect to $x \in [0, d_e]$ coordinate.

Submitting $w(x,t)$ and $\varphi(x,t)$ from Eq. 11 into equilibrium equation Eq. 2 and Eq. 4 respectively. Doing the integration according to Galerkin's approach and part-by-part integration to the resulting function. The weak forms can be derived and the element mass matrices $\mathbf{M}^{(e)b}$ and $\mathbf{M}^{(e)t}$, stiffness matrices $\mathbf{K}^{(e)b}$ and $\mathbf{K}^{(e)t}$, force vectors $\mathbf{F}^{(e)b}$

and $\mathbf{F}^{(e)t}$ for bending and torsion are extracted separately as:

$$\begin{aligned}
\mathbf{M}^{(e)b} &= \rho A \int_0^{d_e} (\mathbf{N}^b)^T \mathbf{N}^b \mathrm{d}x, \\
\mathbf{M}^{(e)t} &= \rho J \int_0^{d_e} (\mathbf{N}^t)^T \mathbf{N}^t \mathrm{d}x, \\
\mathbf{K}^{(e)b} &= \int_0^{d_e} \left[C_1^b \left((\mathbf{N}^b)'' \right)^T (\mathbf{N}^b)'' + (C_2^b - C_4^b) \left((\mathbf{N}^b)''' \right)^T (\mathbf{N}^b)''' + C_3^b \left((\mathbf{N}^b)'''' \right)^T (\mathbf{N}^b)'''' \right] \mathrm{d}x, \\
\mathbf{K}^{(e)t} &= \int_0^{d_e} \left[C_1^t \left((\mathbf{N}^t)' \right)^T (\mathbf{N}^t)' + (C_2^t - C_4^t) \left((\mathbf{N}^t)'' \right)^T (\mathbf{N}^t)'' + C_3^t \left((\mathbf{N}^t)''' \right)^T (\mathbf{N}^t)''' \right] \mathrm{d}x, \\
\mathbf{F}^{(e)b} &= \int_0^{d_e} \overline{f}(x,t) \mathbf{N}^b \mathrm{d}x + f_0 \mathbf{N}^b|_{\partial\Omega_{f_0}} + M_0 (\mathbf{N}^b)'|_{\partial\Omega_{M_0}} + M_1 (\mathbf{N}^b)''|_{\partial\Omega_{M_1}} + M_2 (\mathbf{N}^b)'''|_{\partial\Omega_{M_2}}, \\
\mathbf{F}^{(e)t} &= \int_0^{d_e} \bar{T}(x,t) \mathbf{N}^t \mathrm{d}x + T_0 \mathbf{N}^t|_{\partial\Omega_{T_0}} + T_1 (\mathbf{N}^t)'|_{\partial\Omega_{T_1}} + T_2 (\mathbf{N}^t)''|_{\partial\Omega_{T_2}},
\end{aligned} \tag{13}$$

where superscript ($'$) means partial derivative with respect to coordinate x. The local out-of plane vibration matrices or vector for an element are illustrated by adding bending and torsion cases together, as presented:

$$\mathbf{M}^{(e)} = \mathbf{M}^{(e)b} + \mathbf{M}^{(e)t}, \ \mathbf{K}^{(e)} = \mathbf{K}^{(e)b} + \mathbf{K}^{(e)t}, \ \mathbf{F}^{(e)} = \mathbf{F}^{(e)b} + \mathbf{F}^{(e)t}. \tag{14}$$

3.2. *WFEM for 2D periodic structures*

In this step, the WFEM for 2D periodic structures [61] is introduced. As discussed in Sec. 3.1, the element stiffness and mass matrices along x direction are deduced. Then, the stiffness and mass matrices along y direction can be confirmed by using coordinate transformation matrix [62]. The global mass matrix $\mathbf{M}$ and stiffness matrix $\mathbf{K}$ of a unit cell in the beam grid can be calculated by matrix assembly. Defining that $\hat{\mathbf{u}}$ and $\hat{\mathbf{F}}$ are the amplitudes of nodal harmonic displacement $\mathbf{u}$ and force $\mathbf{F}$ of a unit cell, respectively. As presented in Fig. 1(b), the nodal DOFs ($\hat{\mathbf{u}}$) are divided into corners DOFs ($\hat{\mathbf{u}}_1$, $\hat{\mathbf{u}}_2$, $\hat{\mathbf{u}}_3$) and internal DOFs ($\hat{\mathbf{u}}_\mathrm{I}$). The vectors of corners forces are represented by $\hat{\mathbf{F}}_1$, $\hat{\mathbf{F}}_2$ and $\hat{\mathbf{F}}_3$. Assuming that there are no external forces on the internal DOFs: $\hat{\mathbf{F}}_\mathrm{I} = \mathbf{0}$. The well known dynamical equilibrium equation [3] of a unit cell is written as:

$$(\mathbf{K} - \omega^2 \mathbf{M}) \hat{\mathbf{u}} = \hat{\mathbf{F}}, \tag{15}$$

where $\hat{\mathbf{u}} = [\hat{\mathbf{u}}_1^T, \hat{\mathbf{u}}_2^T, \hat{\mathbf{u}}_3^T, \hat{\mathbf{u}}_\mathrm{I}^T]^T$, $\hat{\mathbf{F}} = [\hat{\mathbf{F}}_1^T, \hat{\mathbf{F}}_2^T, \hat{\mathbf{F}}_3^T, \mathbf{0}^T]^T$. According to the Bloch's theorem, the DOFs' relations and forces' relations can be expressed separately as [61]:

$$\hat{\mathbf{u}} = \mathbf{\Lambda}_R \begin{pmatrix} \hat{\mathbf{u}}_1 \\ \hat{\mathbf{u}}_\mathrm{I} \end{pmatrix}, \qquad \mathbf{\Lambda}_L \hat{\mathbf{F}} = \mathbf{0}, \tag{16}$$

with

$$\mathbf{\Lambda}_R = \begin{bmatrix} \mathbf{I}_s & \mathbf{0} \\ \lambda_y \mathbf{I}_s & \mathbf{0} \\ \lambda_x \mathbf{I}_s & \mathbf{0} \\ \mathbf{0} & \mathbf{I}_I \end{bmatrix}, \qquad \mathbf{\Lambda}_L = \begin{bmatrix} \mathbf{I}_s & \lambda_y^{-1} \mathbf{I}_s & \lambda_x^{-1} \mathbf{I}_s & \mathbf{0} \\ \mathbf{0} & \mathbf{0} & \mathbf{0} & \mathbf{I}_I \end{bmatrix}, \tag{17}$$

where λ_x and λ_y are related to wave-numbers κ_x and κ_y by $\lambda_x = \exp(-\mathrm{i}\kappa_x L_x)$ and $\lambda_y = \exp(-\mathrm{i}\kappa_y L_y)$ respectively, $\mathbf{I}_s$ and $\mathbf{I}_I$ denote the identity matrices of size s and I. Substituting Eq. 16 into Eq. 15 yields:

$$\mathbf{\Lambda}_L (\mathbf{K} - \omega^2 \mathbf{M}) \mathbf{\Lambda}_R \begin{pmatrix} \hat{\mathbf{u}}_1 \\ \hat{\mathbf{u}}_\mathrm{I} \end{pmatrix} = \mathbf{0}. \tag{18}$$

Eq. 18 provides a way to analyze the wave propagation in 2D periodic structures. There exist two different forms to solve this equation: the first one is fixing frequency (ω) and λ_y, all possible solutions for λ_x are sought which correspond to evanescent or propagation waves. The second one is fixing λ_x and λ_y, the values of ω are calculated. In our work, the second form which is called inverse form is used. As shown in Fig. 6(b), the wave-numbers κ_x and κ_y change

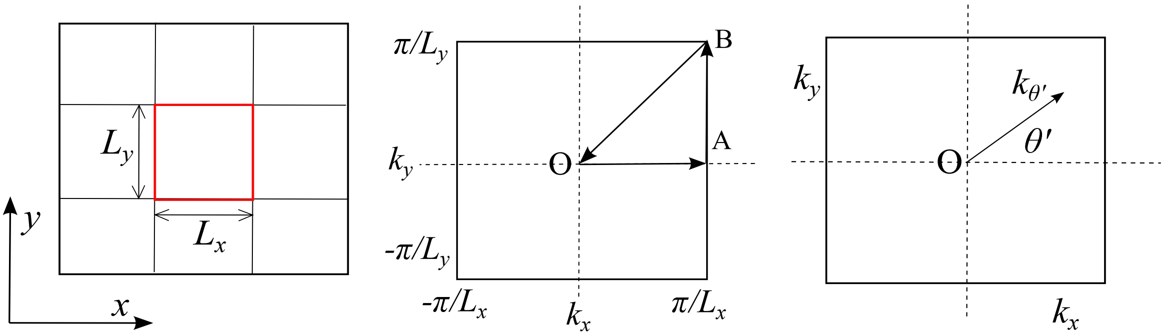

(a) A unit cell in 2D periodic structure.

(b) The first Brillouin zone and the irreducible zone (O–A–B–O).

(c) Plane wave.

Figure 6: Unit cells in 2D periodic structures and the first Brillouin zone. L_x: the length of unit cell along x-direction. L_y: the length of unit cell along y-direction. θ': angle of wave propagation.

within the first Brillouin zone $[-\pi/L_x, \pi/L_x]$ and $[-\pi/L_y, \pi/L_y]$ and are discretised into (κ_x^i, κ_y^j), with κ_x^i being the i-th term, κ_y^j being the j-th term. The corresponding frequencies (ω) are sorted in the ascending order $\omega^{i,j}_{1,2,3,...k,...n}$. The k-th slowness surface is formed by $\omega^{i,j}_k$. The Poynting vector (i.e., energy flow vector) at any point (κ_x, κ_y) is same as the gradient of slowness surface [63]. For the iso-frequency contour of the slowness surface, Poynting vector is normal to the contour curves. This character can be used to determine the direction of wave propagation and non-propagation which is known as the wave beaming effect.

In addition, a convenient 2D representation of the slowness surface is the band structure, which is obtained by plotting the wave-numbers along the contour O–A–B–O as shown in Fig. 6(b). The plane wave propagates with wave-number $\kappa_{\theta'}$ in angle θ' as shown in Fig. 6(c). The band structure can be used to explore the frequency ranges of stop bands and the location where different slowness surfaces touch each other.

4. Numerical applications

Numerical research based on SSG theory is of great significance for understanding the mechanical properties of micro-sized beam grid. In this part, the inverse form of WFEM is applied to analyze the out-of plane vibration of the beam grid. The dynamic behaviors such as band structure, slowness surfaces, energy flow vector fields and wave beaming effects are discussed.

The material of a unit cell in the beam grid is Aluminum with $15a_0$ wide and $20a_0$ high in cross-section, $L_x = 250a_0$ and $L_y = 175a_0$ ($a_0 = 4.04 \times 10^{-10}$m is the lattice parameter). The size of this unit cell is at nano-sized level and the characteristics of non-local interactions in the unit cell can be presented effectively. The Young's modulus $E = 70$ GPa, linear mass density $\rho = 2.7$ g/cm^3, and each branch of the unit cell is meshed into 20 elements. Here should be pointed that, in order to ensure the periodicity of the beam grid, as presented in Fig. 1(b), $m/2$ is added at node $\hat{\mathbf{u}}_1$, $m/4$ is added at $\hat{\mathbf{u}}_2$ and $\hat{\mathbf{u}}_3$, m is added at each internal node $\hat{\mathbf{u}}_\mathrm{I}$, where m is the nodal mass. So the whole beam grid can be obtained by repeating this unit cell. The beam grid contains 20 unit cells along x direction and 20 unit cells along y direction. Here should be pointed that the circular frequency is normalized as ω/ω_0, in which ω_0 is the first nature circular frequency of the unit cell.

4.1. Band structure

Fig. 7(a) shows the four lowest branches of the normalized frequency spectrum along the boundary (O-A-B-O) of the irreducible first Brillouin zone for 2D beam grid. The blue lines represent the results from SSG theory and black lines denote the CT. The curve by SSG is close to the one by CT at low frequency. But the difference between SSG and CT becomes more obvious as frequency increases. On the other hand, the frequency value by SSG is higher than CT at same κ-space position. This phenomenon can be explained as: the potential energy density in SSG theory is a function of strain, first gradient of strain and second gradient of strain, which leads to the dynamical equilibrium equation being a high order partial differential function composed of classical part and non-classical part. Due to

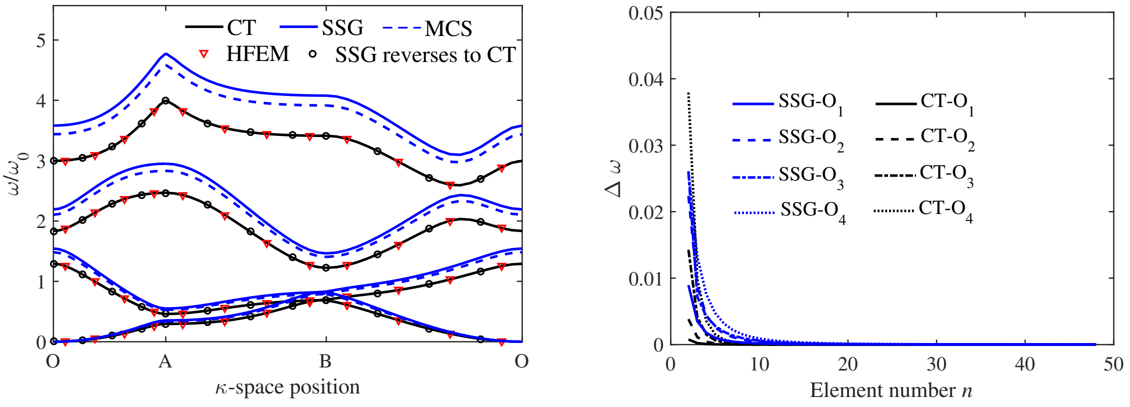

(a) Band structure by SSG and CT and validation.

(b) Convergence of band structure at boundary point O by SSG and CT.

Figure 7: Band structure, validation and convergence. (a): band structure is obtained by plotting the wave-numbers along the contour O–A–B–O. The vertical axis is normalized as ω/ω_0, in which ω_0 is the first nature circular frequency of the unit cell. (b): $\Delta\omega$ is the frequency growth rate. The convergence is guaranteed when the element number n of each branch in the unit cell is 20.

the existence of non-classical parts containing higher-order parameters, the eigenvalue ω calculated by the dynamical equilibrium equation of SSG theory is bigger than the one of CT at same κ-space position. In order to valid the band structure by CT, a linear elastic method called Hierarchical Finite Element Method (HFEM) [64] is used, as shown in Fig. 7(a), the result by HFEM matches CT well. At the same time, when the higher order parameters a_i, b_i and c_i are equal to zero, SSG will reverse to CT. This is also a reasonable way to verify the correctness of the numerical simulation results by SSG theory. On the other hand, a higher-order continuum theory called Modified Couple Stress (MCS) theory is used to compare with SSG theory. For the out-of plane vibration analysis by MCS theory, the bending and torsion dynamic stiffness matrices can be calculated by using Galerkin's approach for the bending strong form [65] and torsion strong form [66] respectively. Then, the global dynamic stiffness matrix can be obtained by matrix assembly. It shows that, at low frequency, the result from SSG theory matches the result from MCS theory. But the discrepancy becomes more obvious as frequency increases. This is because that the curvature tensor is considered in MCS theory, curvature tensor and higher order terms of strain tensor are considered in SSG theory. As we can see, there exists band gap. A possibility to have band gap is to enlarge or change the set of kinematic descriptors on the node [67]. The kinematic descriptors on node 1, 2 and 3 are different from internal node. This is the reason why band gap appears. Fig. 7(b) is about the convergence of the first four frequencies at boundary point O by SSG and CT. The horizontal coordinate is the element number of each branch in the unit cell and the vertical coordinate is the variety of frequency. As shown in Fig. 7(b), the variety of frequency decreases with element number increases and shows the convergence character.

4.2. *Slowness surfaces*

The first three slowness surfaces, as presented in Fig. 8, are studied in the frequency range based on SSG and CT. The 3D surfaces are symmetric with respect to κ_x and κ_y. The slowness surface position by SSG is higher than CT. This phenomenon can be explained by taking the bending wave as an example: assuming the lateral distributed force $\overline{f}(x,t) = 0$ and submitting bending displacement $w(x,t) = w_0 e^{i(\omega t-\kappa x)}$ into Eq. 2, the dynamical equation of bending wave by SSG theory becomes: $C_1^b\kappa^4 + (C_4^b - C_2^b)\kappa^6 + C_3^b\kappa^8 = \rho A\omega^2$, in which the term containing the fourth power of wave-number corresponds to CT. It can be clearly found that the frequency value by SSG is bigger than the value by CT at same κ-space position.

As shown in Fig. 9, in order to calculate the iso-frequency contours, the normalized frequencies are chosen at 0.008 and 0.08 on the first slowness surface, 0.9 and 1.2 on the second slowness surface, 1.9 and 2.1 on the third slowness surface. The direction, perpendicular to the iso-frequency line, indicates the direction of wave propagation and more details will be discussed in Sec. 4.3. At low frequency, the iso-frequency lines by SSG are close to CT. However, there exists a big difference between SSG and CT at higher frequency, which means that the high-order

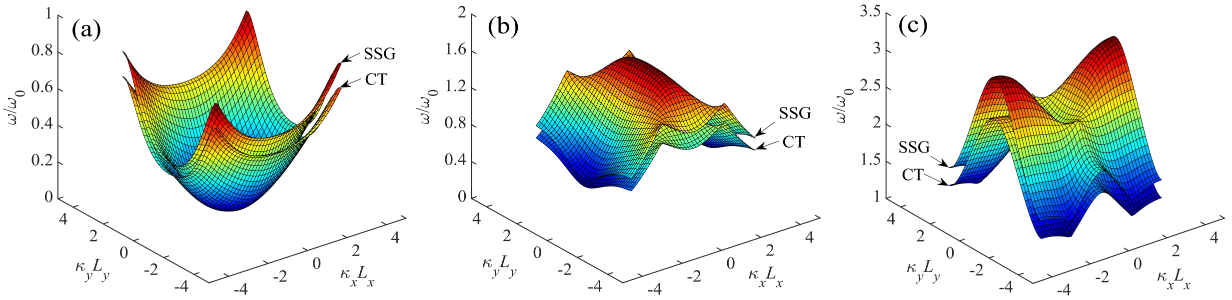

Figure 8: The first three slowness surfaces by SSG and CT. (a): the first slowness surface. (b): the second slowness surface. (d): the third slowness surface. Multiplying the wavenumbers κ_x and κ_y by length L_x and L_y respectively, the wave propagation range is limited into $-\pi$ to π. The vertical axis is normalized by the first nature frequency (ω_0) of the unit cell.

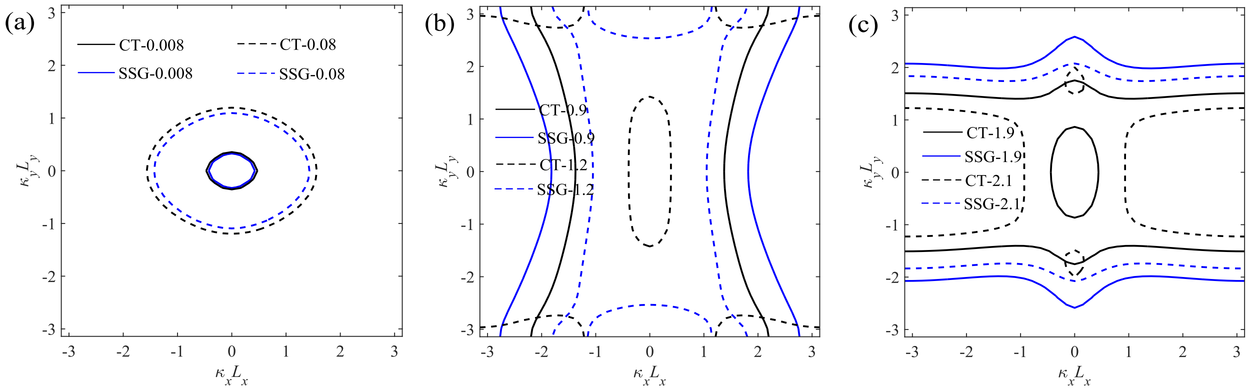

Figure 9: The iso-frequency contour of first three slowness surfaces by SSG and CT. (a): normalized frequencies ω/ω_0 are 0.008 and 0.08. (b): normalized frequencies ω/ω_0 are 0.9 and 1.2. (c): normalized frequencies ω/ω_0 are 1.9 and 2.1. The wave propagation range is limited into $-\pi$ to π.

parameters have a significant influence on the value of iso-frequency contours at higher frequency. What is more, as a set of points of the same frequencies, the iso-frequency contour is also used to explore and describe the energy state on each surface. For example, on the first surface, $\omega/\omega_0 = 0.008$ contour shown in Fig. 9(a) indicates that the waves with same energy exhibit a continuous circular state. As the frequency increases, the energy value increases as well. But on the second surface as shown in Fig. 9(b), waves with the same energy exhibit discontinuities. When $\omega/\omega_0 = 0.9$, the whole iso-frequency contours appear on the left and right sides of the center point. When $\omega/\omega_0 = 1.2$, the majority of iso-frequency contours also appear on the left and right sides of the center point. This phenomena indicates that most waves with the same energy travel in the x direction. On the other hand, on the third surface, the majority of iso-frequency contours are concentrated above and below the center point, which means that, at higher frequency such as $\omega/\omega_0 = 1.9$, most waves with the same energy travel in the y direction.

4.3. Energy flow vector fields

The energy flow vector fields by SSG and CT on the first three slowness surfaces are studied in this part. As shown in Fig. 10, the direction of arrow indicates the direction of energy flow and the length of arrow means the gradient value of energy flow. The blue arrow from SSG and black arrow from CT almost overlap, which indicates that the gradient and direction of energy flow by SSG are basically the same as that by CT at the same κ-space position. At low frequency, as shown in Fig. 10(a), the behavior of beam grid is similar to an homogeneous orthotropic plate where the dynamic energy spreads in all directions and is perpendicular to the iso-frequency contour. As we can see, from the center point to the boundary, the energy increases as the frequency increases and become more dense. The stability of the structure remains the same in all directions. However, at higher frequency such as 0.9, as shown in Fig. 10(b), the directions of majority energy are limited to x direction, which means that there are stop bands in y direction. The

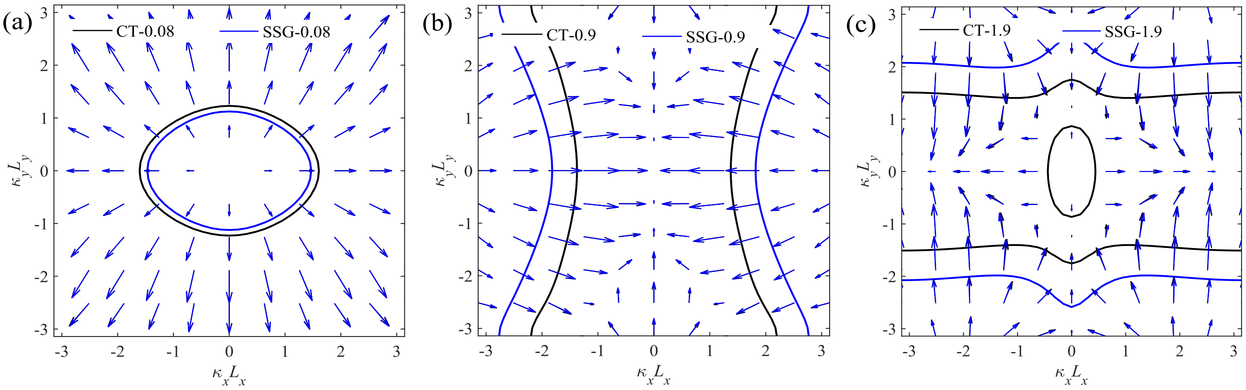

Figure 10: Energy flow vector fields by SSG and CT on the first three slowness surfaces. (a): energy flow vector field on the first slowness surface, normalized frequencies is 0.08. (b): energy flow vector field on the second slowness surface, normalized frequencies is 0.9. (c): energy flow vector field on the third slowness surface, normalized frequencies is 1.9. The direction of arrow indicates the direction of energy flow and the length of arrow means the gradient value of energy flow.

most of the high-energy waves that cause the structure to vibrate strongly propagate in the x direction. The stability of the structure in the x direction is weakened. On the other hand, when normalized frequency is 1.9 as presented in Fig. 10(c), the directions of majority energy are restricted to y direction and stop bands exist in x direction. As a result, the structure becomes unstable in the y direction.

The distance from any point on the iso-frequency contour to the center point of the figure represents the wave number $\kappa_{\theta'}$ with θ' for plane wave propagation. On the first slowness surface, the position of the iso-frequency contour from SSG is located inside the iso-frequency contour from CT, which means that $\kappa_{\theta'}$ from SSG is smaller than the one from CT at same wave propagation angle θ'. Contrast that with the second and third slowness surfaces, whose iso-frequency contour position from SSG is located outside the one from CT, which shows that $\kappa_{\theta'}$ from SSG is bigger than the one from CT.

4.4. *Wave beaming effects*

For further research of wave propagation directivity, the function $\kappa_y = f(\kappa_x)$ is defined for a given iso-frequency contour line in the first quadrant as shown in Fig.10. The wave propagation direction ψ, perpendicular to the iso-frequency contour, can be confirmed by $\psi = \arctan(\mathrm{d}\kappa_y/\mathrm{d}\kappa_x)+\pi/2$ [68]. The frequency dependent directional behavior of the beam grid by CT and SSG can be visualized through polar images as shown in Fig. 11. In the case of ω/ω_0 =0.08 on first slowness surface, wave propagation occurs in all directions which verifies the conclusion in 4.3. The direction of wave propagation under other different frequencies can be predicted as well. It should be pointed out that there exist two directions of wave propagation at some frequencies as shown in Fig. 11(b), Fig. 11(c), Fig. 11(e) and Fig. 11(f). This is because there may be two iso-frequency contours at a certain frequency in the first quadrant, for example as shown in Fig. 10(c) for CT case. Two different directions of wave propagation can be generated with one being primary and another one being secondary. In this work, the primary wave propagation directivity is studied.

In addition, the harmonic displacement fields are explored under Born-von Karman boundary conditions [1, 69]: in damped systems, the response of harmonic displacement is considered approximately independent from boundary conditions. The function of harmonic displacement fields by FE method is expressed as: $[(1 + \mathrm{i}\eta)\mathbf{K}' - \omega^2\mathbf{M}']\hat{\mathbf{u}}' = \hat{\mathbf{F}}'$ [1], in which $\mathbf{K}'$ and $\mathbf{M}'$ are stiffness and mass matrices of the beam grid with 20 unit cells along x direction and 20 unit cells along y direction. Due to the existence of damping loss factor η, the input power from external force rarely reaches the system boundary. So, the response by the above equation is closely approximate to the response of an infinite system. The free boundary condition was chosen for the beam grid in this work. Loss factor η is 0.05 and a harmonic force with unit amplitude is loaded at central place of the structure along z direction.

The results of displacement amplitudes along z direction, normalized with respect to the central point amplitudes (z_c), are presented in Fig. 12 by CT and SSG respectively. The continuous maps are obtained by interpolating the nodal displacements. The white lines on the harmonic displacement field images indicate the range of wave propagation as predicted in Fig. 11. The above results show that the directional patterns of the harmonic displacement response

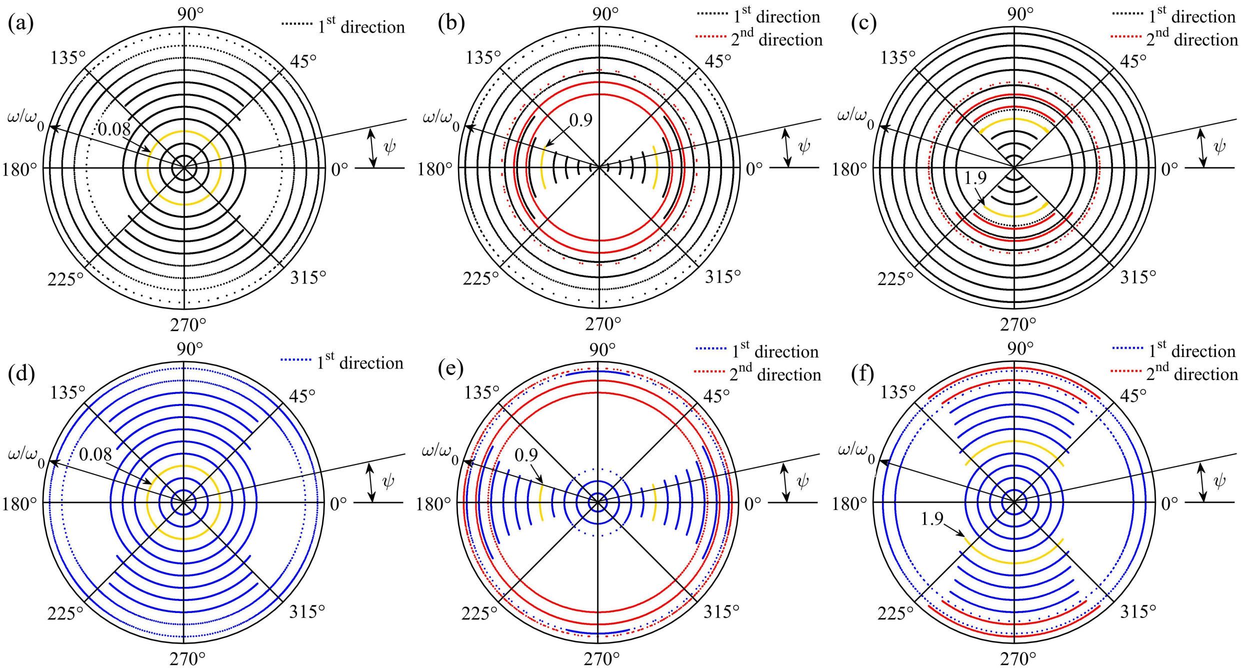

Figure 11: Direction of wave propagation by CT and SSG. (a): the 1st slowness surface by CT. (b): the 2nd slowness surface by CT. (c): the 3rd slowness surface by CT. (d): the 1st slowness surface by SSG. (e): the 2nd slowness surface by SSG. (f): the 3rd slowness surface by SSG. The frequency ω increases from the center of the polar image to the edge. Angular ψ is the range of free wave propagation. Black line: 1st direction. Red line: 2nd direction. Yellow line: wave propagation at a specific frequency.

match the predictions from the energy flow vector fields, as well as the wave propagation directivity analysis. On the other hand, at low frequency, the wave propagation range by SSG is consistent with the one by CT. At high frequency, the wave propagation range by SSG is different from the one by CT. For instance, $\psi = 42°$ by CT, $\psi = 36.1°$ by SSG when frequency is 0.9, while $\psi = 90°$ by CT, $\psi = 104.7°$ by SSG when frequency is 1.9.

Last, the normalized forced response contours is discussed, as shown in Fig. 13, the iso-displacement contours are calculated at position $z/z_c = 0.1$ along z direction by SSG and CT. Here we fix the normalized frequency as 1.9 which is high frequency. The wave spreads in y direction both by SSG and CT which shows the strong and evident beaming in y direction. Due to the existence of high-order parameters that reflect non-local characteristics, the structure exhibits "hardening" property, which leads to the change of wave propagation range. The range of wave propagation by SSG is bigger than the one by CT at same frequency. Furthermore, from the midpoint of the beam grid to the edge in y direction, the range of wave propagation increases first and then decreases by CT. In contrast, the range of wave propagation increases first and then remains unchanged by SSG.

5. Conclusions

In this paper, Second Strain Gradient (SSG) theory is used for the dynamic analysis of a 2D micro-sized beam grid within the Wave Finite Element Method (WFEM) framework. In order to explore the wave propagation characteristics of micro-sized beam grid, firstly, strong formulas of continuum model for out-of plane vibration are deduced based on Hamilton principle. A valuable long-range Lattice Spring Model (LSM), formed by interactions of nearest, next-nearest and next-next-nearest neighbors, is elaborated which provides a reasonable explanation for the SSG model.

Subsequently, the strong formulas are transformed into the weak formulas. The dynamic behaviors of beam grid are analyzed through WFEM. The results show that the existence of non-classical parts containing higher-order parameters can exert stiffness-hardening mechanisms on micro-sized beam grid. The discrepancies between SSG and CT appear at high frequency in band structure, slowness surfaces and iso-frequency contours. The eigenvalue ω from SSG theory is bigger than the one from CT at same k-space position.

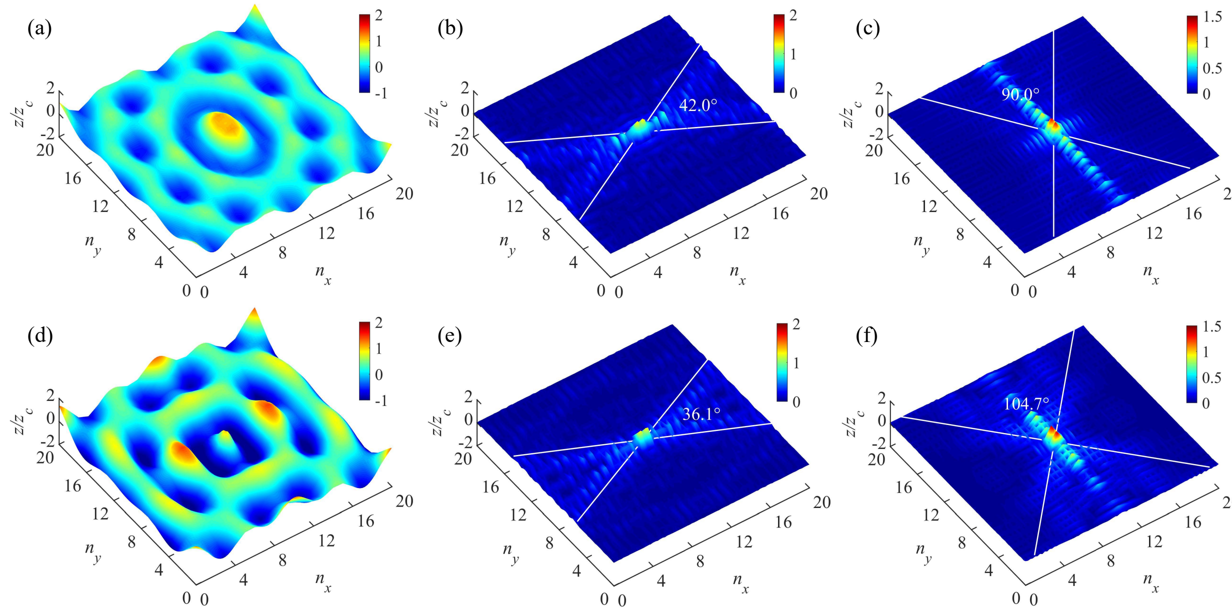

Figure 12: Harmonic displacement field by CT and SSG. (a): ω/ω_0=0.08, ψ = 360° for CT. (b): ω/ω_0=0.9, ψ = 42° for CT. (c): ω/ω_0=1.9, ψ = 90° for CT. (d): ω/ω_0=0.08, ψ = 360° for SSG. (e): ω/ω_0=0.9, ψ = 36.1° for SSG. (f): ω/ω_0=1.9, ψ = 104.7° for SSG. n_x: unit cell number along x direction. n_y: unit cell number along y direction. z_c: central point amplitude. ψ: range of wave propagation under normalized frequency ω/ω_0.

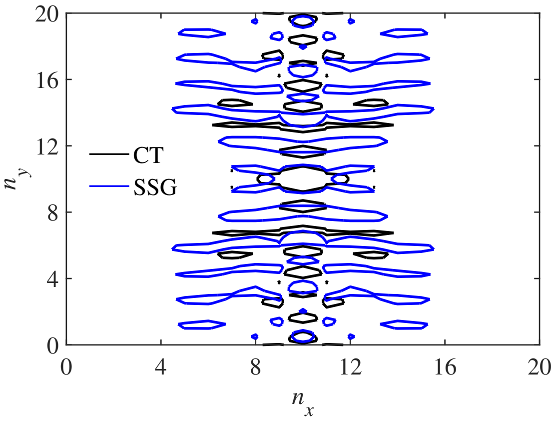

Figure 13: Normalized forced response contours by SSG and CT. n_x: unit cell number along x direction. n_y: unit cell number along y direction. ω/ω_0=1.9 in which ω_0 is first nature frequency of unit cell. z/z_c=0.1 in which z_c is central point amplitude.

On the other hand, the energy flow vector fields on the first three slowness surfaces are studied by SSG and CT. It is found that at low frequency, the behavior of beam grid is similar to an homogeneous orthotropic plate where the dynamic energy spreads in all directions and is normal to the iso-frequency contour. At higher frequency, the directions of majority energy are limited to some specific directions.

Last, the harmonic displacement fields are presented by SSG and CT. Results obtained show that the directional patterns of the harmonic displacement match the predictions from the energy flow vector fields, as well as the wave propagation directivity analysis. There exists an evident beaming phenomenon at high frequency. From the midpoint of the beam grid to the edge, the range of wave propagation increases first and then decreases by CT. However, The range of wave propagation increases first and then remains unchanged by SSG.

Acknowledgements

This work is supported by the LabEx CeLyA (Centre Lyonnais d'Acoustique, ANR-10-LABX-0060) of Université de Lyon. The research of B. Yang is funded by the China Scholarship Council (CSC). The research of C. Droz is funded by the European Commission (WIDEA) under the grant agreement No. 797034.

A. Continuum model vibration analysis for bending

The displacement fields u_1^b (along x direction), u_2^b (along y direction), and u_3^b (along z direction) for micro-sized Euler-Bernoulli beam are:

$$u_1^b = -z\frac{\partial w(x,t)}{\partial x}, \quad u_2^b \ = 0, \quad u_3^b = w(x,t), \tag{19}$$

where $w(x,t)$ means displacement along z direction. Here, non-zero components are considered:

$$\begin{aligned} &\varepsilon_{11} = -z\frac{\partial^2 w(x,t)}{\partial x^2}, \quad \xi_{111} = -z\frac{\partial^3 w(x,t)}{\partial x^3}, \quad \xi_{311} = \xi_{131} = -\frac{\partial^2 w(x,t)}{\partial x^2}, \\ &\zeta_{1111} = -z\frac{\partial^4 w(x,t)}{\partial x^4}, \quad \zeta_{3111} = \zeta_{1311} = \zeta_{1131} = -\frac{\partial^3 w(x,t)}{\partial x^3}, \quad \zeta_{1113} = \frac{\partial^3 w(x,t)}{\partial x^3}. \end{aligned} \tag{20}$$

The beam strain potential energy is illustrated by integrating strain energy density over its volume, one arrives:

$$\begin{aligned} \mathcal{U} &= \int_0^{L_x}\int_A \overline{\mathcal{U}}\mathrm{d}A\mathrm{d}x \\ &= \frac{1}{2}\int_0^{L_x}\left[C_1^b\left(\frac{\partial^2 w(x,t)}{\partial x^2}\right)^2 + C_2^b\left(\frac{\partial^3 w(x,t)}{\partial x^3}\right)^2 + C_3^b\left(\frac{\partial^4 w(x,t)}{\partial x^4}\right)^2 + C_4^b\frac{\partial^2 w(x,t)}{\partial x^2}\frac{\partial^4 w(x,t)}{\partial x^4}\right]\mathrm{d}x, \end{aligned} \tag{21}$$

where C_1^b, C_2^b, C_3^b, C_4^b are expressed in Sec. 2.2. On the other hand, the beam kinetic energy, formed by classical part and non-classical part, is expressed as [70]:

$$\mathcal{T} = \frac{1}{2}\rho\int_\Omega\left(\dot{\mathbf{U}}\cdot\dot{\mathbf{U}} + l_1^2\nabla\dot{\mathbf{U}} : \nabla\dot{\mathbf{U}} + l_2^4\nabla\nabla\dot{\mathbf{U}} \,\vdots\, \nabla\nabla\dot{\mathbf{U}}\right)\mathrm{d}\Omega, \tag{22}$$

where l_1 and l_2 are higher-order length-scale parameters. In our work, the form of kinetic energy is simplified to consider the classical part only [54], which has been discussed in Sec. 2.2. As a result, the beam kinetic energy will be simplified as:

$$\mathcal{T} = \frac{1}{2}\int_0^{L_x}\rho A\left(\frac{\partial w(x,t)}{\partial t}\right)^2\mathrm{d}x, \tag{23}$$

Next, the work done ($\mathcal{W}$) by external classical force ($f(x,t)$, f_0) and higher-order forces (M_0, M_1, M_2) can be calculated under variation framework, one obtains:

$$\begin{aligned} \delta\mathcal{W} = &\int_0^{L_x}\overline{f}(x,t)\delta w(x,t)\mathrm{d}x + f_0\delta w(x,t)|_{x=0}^{L_x} + M_0\delta\left(\frac{\partial w(x,t)}{\partial x}\right)\Bigg|_{x=0}^{L_x} + M_1\delta\left(\frac{\partial^2 w(x,t)}{\partial x^2}\right)\Bigg|_{x=0}^{L_x} \\ &+ M_2\delta\left(\frac{\partial^3 w(x,t)}{\partial x^3}\right)\Bigg|_{x=0}^{L_x}, \end{aligned} \tag{24}$$

Finally, the strong forms of the Euler-Bernoulli micro-beam including governing equation and boundary conditions as shown in Eq. 2 and Eq. 3 are obtained by SSG based on Hamilton's principle:

$$\int_{t_1}^{t_2}(\delta\mathcal{U} - \delta\mathcal{W} - \delta\mathcal{T})\mathrm{d}t = 0, \tag{25}$$

B. Continuum model vibration analysis for torsion

The components of the displacements u_1^t, u_2^t, and u_3^t for torsional micro-beam are expressed as:

$$u_1^t = 0, \quad u_2^t = -z\varphi(x,t), \quad u_3^t = y\varphi(x,t), \tag{26}$$

Ignore zero components of displacement tensors, one arrives:

$$\begin{aligned}
&\varepsilon_{12} = \varepsilon_{21} = -\frac{1}{2}z\frac{\partial\varphi(x,t)}{\partial x}, \varepsilon_{13} = \varepsilon_{31} = \frac{1}{2}y\frac{\partial\varphi(x,t)}{\partial x}, \xi_{112} = -z\frac{\partial^2\varphi(x,t)}{\partial x^2}, \xi_{113} = y\frac{\partial^2\varphi(x,t)}{\partial x^2},\\
&\xi_{123} = \xi_{213} = \frac{\partial\varphi(x,t)}{\partial x}, \xi_{132} = \xi_{312} = \frac{\partial\varphi(x,t)}{\partial x}, \zeta_{1112} = -z\frac{\partial^3\varphi(x,t)}{\partial x^3}, \zeta_{1113} = y\frac{\partial^3\varphi(x,t)}{\partial x^3},\\
&\zeta_{3112} = \zeta_{1312} = \zeta_{1132} = -\frac{\partial^2\varphi(x,t)}{\partial x^2}, \zeta_{2113} = \zeta_{1213} = \zeta_{1123} = \frac{\partial^2\varphi(x,t)}{\partial x^2}.
\end{aligned} \tag{27}$$

Then, the same Hamilton principle method including torsional beam strain potential energy ($\mathcal{U}$), kinetic energy ($\mathcal{T}$) and work done by forces ($\mathcal{W}$) is used as introduced in A. The governing equation and boundary conditions for torsional beam will be illustrated as shown in Eq. 4 and Eq. 5.

C. LSM vibration analysis for bending

As shown in Fig. 3, for the bending case in LSM, the angle of rotation (θ_i) on node n is expressed by displacement fields [34]:

$$\Delta\theta_i = \frac{w_{n+i} - w_n}{id} - \frac{w_n - w_{n-i}}{id}, (i = 1, 2, 3), \tag{28}$$

where θ_1, θ_2 and θ_3 are the angles of rotation from the nearest neighbor, next-nearest neighbor and next-next nearest neighbor interactions respectively. The governing function of motion on node n will be illustrated in z direction based on Lagrange equation [71] as:

$$\frac{\partial\mathcal{L}}{\partial w_n} - f_n = \frac{\mathrm{d}}{\mathrm{d}t}\left(\frac{\partial\mathcal{L}}{\partial\dot{w}_n}\right), \tag{29}$$

where the lagrangian $\mathcal{L}$=$\mathcal{T}$-$\mathcal{U}$, in which:

$$\begin{aligned}
\mathcal{T} &= \frac{1}{2}M\sum_{n=1}^{P}\dot{w}_n^2,\\
\mathcal{U} &= \frac{1}{2}k_1^b\sum_{n=1}^{P}(\Delta\theta_1)^2 + \frac{1}{2}k_2^b\sum_{n=1}^{P}(\Delta\theta_2)^2 + \frac{1}{2}k_3^b\sum_{n=1}^{P}(\Delta\theta_3)^2,
\end{aligned} \tag{30}$$

where P is the nodes number, $\mathcal{T}$ denotes the kinetic energy, $\mathcal{U}$ represents potential energy. The lattice function of motion on node n will be derived by submitting Eq. 28 and Eq. 30 into Eq. 29 as:

$$\begin{aligned}
&\frac{k_1^b}{d^3}(w_{n-2} - 4w_{n-1} + 6w_n - 4w_{n+1} + w_{n+2}) + \frac{k_2^b}{(2d)^3}(w_{n-4} - 4w_{n-2} + 6w_n - 4w_{n+2} + w_{n+4})\\
&+ \frac{k_3^b}{(3d)^3}(w_{n-6} - 4w_{n-3} + 6w_n - 4w_{n+3} + w_{n+6}) - f_n = M\frac{\mathrm{d}^2 w_n(t)}{\mathrm{d}t^2}.
\end{aligned} \tag{31}$$

Hereafter, the continuum function $w(x,t)$ from LSM $w_n(t)$ can be calculated based on Fourier series transform method. The process is introduced as [58]:

(1) Defining an assumption that $w_n(t)$ is the Fourier constant of $\widehat{w}(\kappa,t)$:

$$\widehat{w}(\kappa,t) = \sum_{n=-\infty}^{+\infty} w_n(t)e^{-i\kappa x_n} = \mathcal{F}_\Delta\left(w_n(t)\right), \tag{32}$$

where $\mathcal{F}_\Delta$ is the Fourier series transform.

(2) Taylor series expansion is used based on the limitation of $d \to 0$:

$$\widetilde{w}(\kappa, t) = \lim_{d \to 0} \widehat{w}(\kappa, t), \tag{33}$$

(3) Defining $\mathcal{F}^{-1}$ as inverse Fourier transform:

$$w(x, t) = \frac{1}{2\pi} \int_{-\infty}^{+\infty} \widetilde{w}(x, t) e^{\mathrm{i}\kappa x} \mathrm{d}\kappa = \mathcal{F}^{-1}\left(\widetilde{w}(x, t)\right), \tag{34}$$

in which $x_n = dn$, κ is defined as wavenumber. Multiplying Eq. (31) by $e^{-i\kappa nd}$, and n changes from $-\infty$ to $+\infty$. Afterwards, Eq. (31) can be expressed as:

$$\begin{aligned}
&\frac{k_1^b}{d^3} \sum_{n=-\infty}^{+\infty} e^{-i\kappa nd} \left(w_{n-2} - 4w_{n-1} + 6w_n - 4w_{n+1} + w_{n+2}\right) + \frac{k_2^b}{(2d)^3} \sum_{n=-\infty}^{+\infty} e^{-i\kappa nd} \left(w_{n-4} - 4w_{n-2}\right. \\
&\left.+6w_n - 4w_{n+2} + w_{n+4}\right) + \frac{k_3^b}{(3d)^3} \sum_{n=-\infty}^{+\infty} e^{-i\kappa nd} \left(w_{n-6} - 4w_{n-3} + 6w_n - 4w_{n+3} + w_{n+6}\right) \\
&- \sum_{n=-\infty}^{+\infty} e^{-i\kappa nd} f_n = M \sum_{n=-\infty}^{+\infty} e^{-i\kappa nd} \frac{\mathrm{d}^2 w_n(t)}{\mathrm{d}t^2}.
\end{aligned} \tag{35}$$

Then, the first three parts in the left side of the equation above are presented as:

$$\begin{aligned}
&\frac{k_1^b}{d^3} \left[e^{-2i\kappa d} \sum_{m=-\infty}^{+\infty} e^{-i\kappa md} w_m - 4e^{-i\kappa d} \sum_{j=-\infty}^{+\infty} e^{-i\kappa jd} w_j + 6 \sum_{n=-\infty}^{+\infty} e^{-i\kappa nd} w_n - 4e^{i\kappa d} \sum_{p=-\infty}^{+\infty} e^{-i\kappa pd} w_p \right. \\
&\left. + e^{2i\kappa d} \sum_{q=-\infty}^{+\infty} e^{-i\kappa qd} w_q \right] + \frac{k_1^b}{(2d)^3} \left[e^{-4i\kappa d} \sum_{m=-\infty}^{+\infty} e^{-i\kappa md} w_m - 4e^{-2i\kappa d} \sum_{j=-\infty}^{+\infty} e^{-i\kappa jd} w_j + 6 \sum_{n=-\infty}^{+\infty} e^{-i\kappa nd} w_n \right. \\
&\left. - 4e^{2i\kappa d} \sum_{p=-\infty}^{+\infty} e^{-i\kappa pd} w_p + e^{4i\kappa d} \sum_{q=-\infty}^{+\infty} e^{-i\kappa qd} w_q \right] + \frac{k_1^b}{(3d)^3} \left[e^{-6i\kappa d} \sum_{m=-\infty}^{+\infty} e^{-i\kappa md} w_m - 4e^{-3i\kappa d} \sum_{j=-\infty}^{+\infty} e^{-i\kappa jd} w_j \right. \\
&\left. + 6 \sum_{n=-\infty}^{+\infty} e^{-i\kappa nd} w_n - 4e^{3i\kappa d} \sum_{p=-\infty}^{+\infty} e^{-i\kappa pd} w_p + e^{6i\kappa d} \sum_{q=-\infty}^{+\infty} e^{-i\kappa qd} w_q \right].
\end{aligned} \tag{36}$$

The definition in Eq. (32) is used here, and Eq. (36) can be shown as:

$$\begin{aligned}
&\frac{4k_1^b}{d^3} \left[-2\sin^2\left(\frac{\kappa d}{2}\right) \right]^2 \hat{w}(\kappa, t) + \frac{4k_2^b}{(2d)^3} \left[-8\sin^2\left(\frac{\kappa d}{2}\right) + 8\sin^4\left(\frac{\kappa d}{2}\right) \right]^2 \hat{w}(\kappa, t) \\
&+ \frac{4k_3^b}{(3d)^3} \left[-18\sin^2\left(\frac{\kappa d}{2}\right) + 48\sin^4\left(\frac{\kappa d}{2}\right) - 32\sin^6\left(\frac{\kappa d}{2}\right) \right]^2 \hat{w}(\kappa, t).
\end{aligned} \tag{37}$$

Next, step 2 in Eq. (33) is utilized in sine function form at the point 0. Submitting Eq. (37) into Eq. (35), one arrives:

$$\begin{aligned}
&L_4^b \kappa^4 \tilde{w}(\kappa, t) - L_6^b \kappa^6 \tilde{w}(\kappa, t) + L_8^b \kappa^8 \tilde{w}(\kappa, t) - o(L_j^b \kappa^j \tilde{w}(\kappa, t)) - \mathcal{F}\left(\overline{f}(x, t)\right) \\
&= \rho A \frac{\partial^2 \tilde{w}(\kappa, t)}{\partial t^2}, (j = 10, 12, ...),
\end{aligned} \tag{38}$$

where L_4^b, L_6^b, L_8^b, L_j^b are expressed in Sec. 2.3

Eq. (38) will be re-expressed based on step 3 in Eq. (34):

$$\begin{aligned}
&L_4^b \mathcal{F}^{-\mathbf{1}}(\kappa^4 \tilde{w}(\kappa, t)) - L_6^b \mathcal{F}^{-\mathbf{1}}(\kappa^6 \tilde{w}(\kappa, t)) + L_8^b \mathcal{F}^{-\mathbf{1}}(\kappa^8 \tilde{w}(\kappa, t)) - o\left(L_j^b \mathfrak{F}^{-\mathbf{1}}(\kappa^j \tilde{w}(\kappa, t))\right) - \overline{f}(x, t) \\
&= \rho A \frac{\partial^2 \mathcal{F}^{-\mathbf{1}}(\tilde{w}(\kappa, t))}{\partial t^2}.
\end{aligned} \tag{39}$$

in which:

$$\mathcal{F}^{-1}(\kappa^4\tilde{w}(\kappa,t)) = \frac{\partial^4 w(x,t)}{\partial x^4}, \quad \mathcal{F}^{-1}(\kappa^6\tilde{w}(\kappa,t)) = -\frac{\partial^6 w(x,t)}{\partial x^6}, \quad \mathcal{F}^{-1}(\kappa^8\tilde{w}(\kappa,t)) = \frac{\partial^8 w(x,t)}{\partial x^8}. \tag{40}$$

Finally, the dynamic continuum function $w(x,t)$ will be written as:

$$L_4^b\frac{\partial^4 w(x,t)}{\partial x^4} + L_6^b\frac{\partial^6 w(x,t)}{\partial x^6} + L_8^b\frac{\partial^8 w(x,t)}{\partial x^8} + o\left(L_i^b\frac{\partial^j w(x,t)}{\partial x^j}\right) - \overline{f}(x,t) = \rho A\frac{\partial^2 w(x,t)}{\partial t^2}. \tag{41}$$

D. LSM vibration analysis for torsion

The torsional lattice function of motion $\varphi_n(t)$ on node n is expressed as:

$$k_1^t(\varphi_{n-1} - 2\varphi_n + \varphi_{n+1}) + k_2^t(\varphi_{n-2} - 2\varphi_n + \varphi_{n+2}) + k_3^t(\varphi_{n-3} - 2\varphi_n - \varphi_{n+3}) - T_n = \frac{MJ}{A}\frac{\mathrm{d}^2\varphi_n(t)}{\mathrm{d}t^2}. \tag{42}$$

In order to obtain the dynamic continuum function $\varphi(x,t)$, the same method is used as shown in C. Multiplying Eq. (42) by $e^{-\iota\kappa nd}$ with n from $-\infty$ to $+\infty$, Eq. (42) will be expressed as:

$$\begin{aligned} &k_1^t\sum_{n=-\infty}^{+\infty} e^{-\iota\kappa nd}(\varphi_{n-1} - 2\varphi_n + \varphi_{n+1}) + k_2^t\sum_{n=-\infty}^{+\infty} e^{-\iota\kappa nd}(\varphi_{n-2} - 2\varphi_n + \varphi_{n+2}) \\ &+ k_3^t\sum_{n=-\infty}^{+\infty} e^{-\iota\kappa nd}(\varphi_{n-3} - 2\varphi_n + \varphi_{n+3}) - \sum_{n=-\infty}^{+\infty} e^{-\iota\kappa nd}T_n = \frac{MJ}{A}\sum_{n=-\infty}^{+\infty} e^{-\iota\kappa nd}\frac{\mathrm{d}^2\varphi_n(t)}{\mathrm{d}t^2}. \end{aligned} \tag{43}$$

Employing the same mathematical calculations and Fourier series transform approach as explained in C: (1) Defining an assumption that $\varphi_n(t)$ is the Fourier constant of $\widehat{\varphi}(\kappa,t)$, (2) The expansion of Taylor series is used based on the limitation of $d \to 0$, (3) Defining $\mathcal{F}^{-1}$ as inverse Fourier transform. Then, the dynamic continuum function $\varphi(x,t)$ is illustrated as:

$$\begin{aligned} &L_2^t\frac{\partial^2\varphi(x,t)}{\partial x^2} + L_4^t\frac{\partial^4\varphi(x,t)}{\partial x^4} + L_6^t\frac{\partial^6\varphi(x,t)}{\partial x^6} + o\left(L_j^t\frac{\partial^j\varphi(x,t)}{\partial x^i}\right) - \overline{T}(x,t) \\ &= \rho J\frac{\mathrm{d}^2\varphi(x,t)}{\mathrm{d}t^2}, (j = 8, 10, ...). \end{aligned} \tag{44}$$

with L_2^t, L_4^t, L_6^t, L_j^t are shown in Sec. 2.3

References

[1] R. S. Langley, The response of two-dimensional periodic structures to point harmonic forcing, Journal of Sound and Vibration 197 (1996) 447–469.

[2] A. C. Eringen, D. G. B. Edelen, On nonlocal elasticity, International Journal of Engineering Science 10 (1972) 233–248.

[3] C. Droz, C. Zhou, M. N. Ichchou, J. P. Lainé, A hybrid wave-mode formulation for the vibro-acoustic analysis of 2d periodic structures, Journal of Sound and Vibration 363 (2016) 285–303.

[4] P. Zhao, K. Zhang, C. Zhao, L. Qi, Z. Deng, In-plane wave propagation analysis for waveguide design of hexagonal lattice with koch snowflake, International Journal of Mechanical Sciences 209 (2021) 106724.

[5] Y. Li, S. Yan, H. Li, Wave propagation of 2d elastic metamaterial with rotating squares and hinges, International Journal of Mechanical Sciences (2021) 107037.

[6] S. Halkjær, O. Sigmund, J. Jensen, Maximizing band gaps in plate structures, Structural and Multidisciplinary Optimization 32 (2006) 263–75.

[7] D. Yu, Y. Liu, J. Qiu, Complete flexural vibration band gaps in membrane-like lattice structures, Physics Letters A 357 (2006) 154–8.

[8] Z. J. Yang, R. Jiang, X. L. Zhuo, Y. M. Xie, J. F. Wang, H. Q. Lin, Dielectric nanoresonators for light manipulation, Physics Reports 701 (2017) 1–50.

[9] J. Pei, T. Thundat, Glucose biosensor based on the microcantilever, Analytical Chemistry 76 (2004) 292–297.

[10] F. Ebrahimi, A. Dabbagh, Nsgt-based acoustical wave dispersion characteristics of thermo-magnetically actuated double-nanobeam systems, Struct. Eng. Mech. 68 (6) (2018) 701–711.

[11] F. Ebrahimi, A. Dabbagh, A novel porosity-based homogenization scheme for propagation of waves in axially-excited fg nanobeams, Advances in nano research 7 (6) (2019) 379–390.

[12] F. Ebrahimi, A. Dabbagh, Wave dispersion characteristics of heterogeneous nanoscale beams via a novel porosity-based homogenization scheme, The European Physical Journal Plus 134 (4) (2019) 1–8.

[13] F. Ebrahimi, A. Dabbagh, T. Rabczuk, F. Tornabene, Analysis of propagation characteristics of elastic waves in heterogeneous nanobeams employing a new two-step porosity-dependent homogenization scheme, Advances in nano research 7 (2) (2019) 135.

[14] F. Ebrahimi, A. Dabbagh, Magnetic field effects on thermally affected propagation of acoustical waves in rotary double-nanobeam systems, Waves in Random and Complex Media 31 (1) (2021) 25–45.

[15] A. Dabbagh, A. Rastgoo, F. Ebrahimi, Post-buckling analysis of imperfect multi-scale hybrid nanocomposite beams rested on a nonlinear stiff substrate, Engineering with Computers (2020) 1–14.

[16] H.-T. Thai, T. P. Vo, T.-K. Nguyen, S.-E. Kim, A review of continuum mechanics models for size-dependent analysis of beams and plates, Composite Structures 177 (2017) 196–219.

[17] B. Zhang, H. Li, L. Kong, J. Wang, H. Shen, Strain gradient differential quadrature beam finite elements, Computers & Structures 218 (2019) 170–189.

[18] M. R. Barati, Vibration analysis of porous fg nanoshells with even and uneven porosity distributions using nonlocal strain gradient elasticity, Acta Mechanica 229 (3) (2018) 1183–1196.

[19] R. E. Miller, V. B. Shenoy, Size-dependent elastic properties of nano-sized structural elements, Nanotechnology 11 (3) (2000) 139.

[20] R. Toupin, Elastic materials with couple-stresses, Archive for rational mechanics and analysis 11 (1) (1962) 385–414.

[21] R. Mindlin, H. Tiersten, Effects of couple-stresses in linear elasticity, Tech. rep., Columbia Univ New York (1962).

[22] W. Koiter, Couple-stresses in the theory of elasticity, i and ii, prec, Roy. Netherlands Acad. Sci. B 67 (1964) 0964.

[23] F. Yang, A. Chong, D. C. C. Lam, P. Tong, Couple stress based strain gradient theory for elasticity, International journal of solids and structures 39 (10) (2002) 2731–2743.

[24] R. D. Mindlin, Micro-structure in linear elasticity, Archive for Rational Mechanics and Analysis 16 (1964) 51–78.

[25] H. M. Shodja, F. Ahmadpoor, T. A., Calculation of the additional constants for fcc materials in second strain gradient elasticity: behavior of a nano-size bernoulli-euler beam with surface effects, Applied Mechanics 72 (2) (2010) 021008.

[26] R. D. Mindlin, Second gradient of strain and surface tension in linear elasticity, International Journal of Solids and Structures (1965) 147–438.

[27] A. C. Eringen, Linear theory of micropolar elasticity, Journal of Mathematics and Mechanics (1966) 909–923.

[28] E. Kröner, Elasticity theory of materials with long range cohesive forces, International Journal of Solids and Structures 3 (5) (1967) 731–742.

[29] M. E. Gurtin, A. I. Murdoch, Surface stress in solids, International Journal of Solids and Structures 14 (6) (1978) 431–440.

[30] M. Delfani, S. Shojaeimanesh, V. Bagherpour, Effective shear modulus of functionally graded fibrous composites in second strain gradient elasticity, Journal of Elasticity 137 (1) (2019) 43–62.

[31] S. Khakalo, J. Niiranen, Form ii of mindlin's second strain gradient theory of elasticity with a simplification: For materials and structures from nano-to macro-scales, European Journal of Mechanics-A/Solids 71 (2018) 292–319.

[32] I. Esen, Response of a micro-capillary system exposed to a moving mass in magnetic field using nonlocal strain gradient theory, International Journal of Mechanical Sciences 188 (2020) 105937.

[33] M. S. Nematollahi, H. Mohammadi, Geometrically nonlinear vibration analysis of sandwich nanoplates based on higher-order nonlocal strain gradient theory, International Journal of Mechanical Sciences 156 (2019) 31–45.

[34] B. Yang, C. Droz, A. M. Zine, M. N. Ichchou, Dynamic analysis of second strain gradient elasticity through a wave finite element approach, Composite Structures (2020).

[35] G. Rosi, N. Auffray, Anisotropic and dispersive wave propagation within strain-gradient framework, Wave Motion 63 (2016) 120–134.

[36] D. Polyzos, D. Fotiadis, Derivation of mindlin's first and second strain gradient elastic theory via simple lattice and continuum models, International Journal of Solids and Structures 49 (2012) 470–480.

[37] A. F. Russillo, G. Failla, Wave propagation in stress-driven nonlocal rayleigh beam lattices, International Journal of Mechanical Sciences 215 (2022) 106901.

[38] X.-D. Hu, G.-F. Zhao, X.-F. Deng, Y.-F. Hao, L.-F. Fan, G.-W. Ma, J. Zhao, Application of the four-dimensional lattice spring model for blasting wave propagation around the underground rock cavern, Tunnelling and Underground Space Technology 82 (2018) 135–147.

[39] A. Suiker, A. Metrikine, R. De Borst, Comparison of wave propagation characteristics of the cosserat continuum model and corresponding discrete lattice models, International Journal of Solids and Structures 38 (9) (2001) 1563–1583.

[40] J. Zhu, G. Zhao, X. Zhao, J. Zhao, Validation study of the distinct lattice spring model (dlsm) on p-wave propagation across multiple parallel joints, Computers and Geotechnics 38 (2) (2011) 298–304.

[41] J. Eilbeck, G. McGuire, Numerical study of the regularized long-wave equation i: numerical methods, Journal of Computational Physics 19 (1) (1975) 43–57.

[42] R. Glowinski, C.-H. Li, J.-L. Lions, A numerical approach to the exact boundary controllability of the wave equation (i) dirichlet controls: Description of the numerical methods, Japan Journal of Applied Mathematics 7 (1) (1990) 1–76.

[43] W. J. Zhou, M. N. Ichchou, O. Bareille, Finite element techniques for calculations of wave modes in one-dimensional structural waveguides, Structural control and Health monitoring 18 (7) (2011) 737–751.

[44] J. M. Mencik, M. N. Ichchou, Wave finite elements in guided elastodynamics with internal fluid, International Journal of Solids and Structures 44 (2007) 2148–2167.

[45] C. Droz, J. P. Lainé, M. N. Ichchou, G. Inquiété, A reduced formulation for the free-wave propagation analysis in composite structures, Composite Structures 113 (2014) 134–144.

[46] D. Mead, A general theory of harmonic wave propagation in linear periodic systems with multiple coupling, Journal of Sound and Vibration 27 (1973) 235–260.

[47] D. Duhamel, B. R. Mace, M. Brennan, Finite element analysis of the vibrations of waveguides and periodic structures, Journal of Sound and Vibration 294 (2006) 205–220.

[48] M. Collet, M. Ouisse, M. Ruzzene, M. Ichchou, Floquet bloch decomposition for the computation of dispersion of two-dimensional periodic, damped mechanical systems, International Journal of Solids and Structures 48 (2011) 37–48.

[49] W. Zhou, M. Ichchou, Wave propagation in mechanical waveguide with curved members using wave finite element solution, Computer Methods in Applied Mechanics and Engineering 199 (2010) 2099–2109.

[50] F. Errico, M. Ichchou, S. De Rosa, O. Bareille, F. Franco, The modelling of the flow-induced vibrations of periodic flat and axial-symmetric structures with a wave-based method, Journal of Sound and Vibration 424 (2018) 32–47.

[51] R. F. Boukadia, E. Deckers, C. Claeys, M. Ichchou, W. Desmet, A wave-based optimization framework for 1d and 2d periodic structures, Mechanical Systems and Signal Processing 139 (2020) 106603.

[52] O. A. Kandil, E. F. Sheta, Coupled and uncoupled bending-torsion response of twin-tail buffet, Journal of Fluids and Structures 12 (1998) 677–701.

[53] G. Rosi, L. Placidi, N. Auffray, On the validity range of strain-gradient elasticity: a mixed static-dynamic identification procedure, European Journal of Mechanics-A/Solids 69 (2018) 179–191.

[54] V. Balobanov, J. Niiranen, Locking-free variational formulations and isogeometric analysis for the timoshenko beam models of strain gradient and classical elasticity, Computer Methods in Applied Mechanics and Engineering 339 (2018) 137–159.

[55] V. Tarasov, Lattice model with nearest-neighbor and next-nearest-neighbor interactions for gradient elasticity, Discontinuity, Nonlinearity, and Complexity 4 (2015) 11–23.

[56] M. Asghari, S. A. Momeni, R. Vatankhah, The second strain gradient theory-based timoshenko beam model, Journal of Vibration and Control 23 (13) (2015) 2155–2166.

[57] S. A. Momeni, M. Asghari, The second strain gradient functionally graded beam formulation, Composite Structures 188 (2018) 15–24.

[58] V. E. Tarasov, Continuous limit of discrete systems with long-range interaction, Journal of Physics A 39 (48) (2006) 14895–14910.

[59] J. Q. Zhao, P. Zeng, B. Pan, Improved hermite finite element smoothing method for full-field strain measurement over arbitrary region of interest in digital image correlation, Optics and Lasers in Engineering 50 (2012) 1662–1671.

[60] I. Bennamia, A. Badereddine, T. Zebbiche, Measurement of vibrations of composite wings using high-order finite element beam, Journal of Measurements in Engineering 6 (2018) 143–154.

[61] C. Zhou, J. Lainé, M. Ichchou, A. Zine, Multi-scale modelling for two-dimensional periodic structures using a combined mode/wave based approach, Computers and Structures 154 (2015) 145–162.

[62] J. Murín, V. Kutiš, V. Královič, T. Sedlár, 3d beam finite element including nonuniform torsion, Procedia Engineering 48 (2012) 436–444.

[63] R. S. Langley, On the modal density and energy flow characteristics of periodic structures, Journal of Sound and Vibration 2 (1994) 491–511.

[64] N. S. Bardell, The application of symbolic computing to the hierarchical finite element method, International Journal of Numerical Methods in Engineering 28 (1989) 1181–1204.

[65] A. M. Dehrouyeh-Semnani, M. Nikkhah-Bahrami, The influence of size-dependent shear deformation on mechanical behavior of microstructures-dependent beam based on modified couple stress theory, Composite Structures 123 (2015) 325–336.

[66] M. Ö. Yayli, Torsional vibrations of restrained nanotubes using modified couple stress theory, Microsystem Technologies 24 (8) (2018) 3425–3435.

[67] M. G. El Sherbiny, L. Placidi, Discrete and continuous aspects of some metamaterial elastic structures with band gaps, Archive of Applied Mechanics 88 (10) (2018) 1725–1742.

[68] M. Ruzzene, F. Scarpa, F. Soranna, Wave beaming effects in two-dimensional cellular structures, Smart Materials and Structures 12 (2003) 363–372.

[69] V. Cotoni, R. Langley, P. Shorter, A statistical energy analysis subsystem formulation using finite element and periodic structure theory, Journal of Sound and Vibration 318 (2008) 1077–1108.

[70] S. Khakalo, J. Niiranen, Form ii of mindlin's second strain gradient theory of elasticity with a simplification: For materials and structures from nano- to macro-scales, European Journal of Mechanics / A Solids 71 (2018) 292–319.

[71] M. Attar, A. Karrech, K. Regenauer Lieb, Non-linear analysis of beam-like structures on unilateral foundations: A lattice spring model, International Journal of Solids and Structures 88 (2016) 192–214.